The Astronomical Journal, 164:85 (17pp), 2022 September https://doi.org/10.3847/1538-3881/ac7ce5
© 2022. The Author(s). Published by the American Astronomical Society.
OPEN ACCESS

The Open Cluster Chemical Abundances and Mapping Survey. VI. Galactic Chemical Gradient Analysis from APOGEE DR17

Natalie Myers[1], John Donor[1], Taylor Spoo[1], Peter M. Frinchaboy[1], Katia Cunha[2,3], Adrian M. Price-Whelan[4], Steven R. Majewski[5], Rachael L. Beaton[6,7], Gail Zasowski[8], Julia O'Connell[1], Amy E. Ray[1], Dmitry Bizyaev[9,10], Cristina Chiappini[11], D. A. García-Hernández[12,13], Doug Geisler[14,15,21], Henrik Jönsson[16], Richard R. Lane[17], Penélope Longa-Peña[18], Ivan Minchev[11], Dante Minniti[19,20], Christian Nitschelm[18], and A. Roman-Lopes[21]
[1] Department of Physics and Astronomy, Texas Christian University, TCU Box 298840 Fort Worth, TX 76129, USA; n.myers@tcu.edu
[2] Observatório Nacional, Rua General José Cristino, 77, Rio de Janeiro, RJ 20921-400, Brazil
[3] Steward Observatory, University of Arizona, 933 North Cherry Avenue, Tucson, AZ 85721-0065, USA
[4] Center for Computational Astrophysics, Flatiron Institute, 162 Fifth Avenue, New York, NY 10010, USA
[5] Department of Astronomy, University of Virginia, Charlottesville, VA 22904-4325, USA
[6] Department of Astrophysical Sciences, Princeton University, 4 Ivy Lane, Princeton, NJ 08544, USA
[7] The Observatories of the Carnegie Institution for Science, 813 Santa Barbara Street., Pasadena, CA 91101, USA
[8] Department of Physics & Astronomy, University of Utah, 115 S. 1400 E., Salt Lake City, UT 84112, USA
[9] Apache Point Observatory and New Mexico State University, P.O. Box 59, Sunspot, NM, 88349-0059, USA
[10] Sternberg Astronomical Institute, Moscow State University, Moscow, Russia
[11] Leibniz-Institut für Astrophysik Potsdam (AIP), An der Sternwarte 16, D-14482 Potsdam, Germany
[12] Instituto de Astrofísica de Canarias, Vía Láctea S/N, E-38205 La Laguna, Tenerife, Spain
[13] Universidad de La Laguna, Departamento de Astrofísica, E-30206 La Laguna, Tenerife, Spain
[14] Departamento de Astronomía, Universidad de Concepción, Casilla 160-C, Concepción, Chile
[15] Instituto de Investigación Multidisciplinario en Ciencia y Tecnología, Universidad de La Serena, Avenida Raúl Bitrán S/N, La Serena, Chile
[16] Materials Science and Applied Mathematics, Malmö University, SE-205 06 Malmö, Sweden
[17] Centro de Investigación en Astronomía, Universidad Bernardo O'Higgins, Avenida Viel 1497, Santiago, Chile
[18] Centro de Astronomía (CITEVA), Universidad de Antofagasta, Avenida Angamos 601, Antofagasta 1270300, Chile
[19] Departamento de Ciencias Fisicas, Facultad de Ciencias Exactas, Universidad Andres Bello, Av. Fernandez Concha 700, Las Condes, Santiago, Chile
[20] Vatican Observatory, I-00120 Vatican City State, Italy
[21] Department of Astronomy, Universidad La Serena, La Serena, Chile
Received 2022 February 14; revised 2022 June 15; accepted 2022 June 27; published 2022 August 8

Abstract

The goal of the Open Cluster Chemical Abundances and Mapping (OCCAM) survey is to constrain key Galactic dynamic and chemical evolution parameters by the construction and analysis of a large, comprehensive, uniform data set of infrared spectra for stars in hundreds of open clusters. This sixth contribution from the OCCAM survey presents analysis of SDSS/APOGEE Data Release 17 (DR17) results for a sample of stars in 150 open clusters, 94 of which we designate to be "high-quality" based on the appearance of their color–magnitude diagram. We find the APOGEE DR17-derived [Fe/H] values to be in good agreement with those from previous high-resolution spectroscopic open cluster abundance studies. Using a subset of the high-quality sample, the Galactic abundance gradients were measured for 16 chemical elements, including [Fe/H], for both Galactocentric radius (R_{GC}) and guiding center radius (R_{guide}). We find an overall Galactic [Fe/H] versus R_{GC} gradient of -0.073 ± 0.002 dex kpc^{-1} over the range of $6 > R_{GC} < 11.5$ kpc, and a similar gradient is found for [Fe/H] versus R_{guide}. Significant Galactic abundance gradients are also noted for O, Mg, S, Ca, Mn, Na, Al, K, and Ce. Our large sample additionally allows us to explore the evolution of the gradients in four age bins for the remaining 15 elements.

Unified Astronomy Thesaurus concepts: Open star clusters (1160); Galactic abundances (2002); Milky Way evolution (1052); Chemical abundances (224)

Supporting material: machine-readable tables

1. Introduction

Open clusters are key, age-datable tracers that have long been used to explore chemical trends in the Galactic disk. Since the early work of Janes (1979), numerous studies have advanced the field, particularly over the past 15 yr (e.g., Bragaglia et al. 2008; Sestito et al. 2008; Friel et al. 2010; Carrera & Pancino 2011; Yong et al. 2012; Frinchaboy et al. 2013; Netopil et al. 2016, 2022; Cunha et al. 2016; Reddy et al. 2016; Magrini et al. 2017; Donor et al. 2020; Spina et al. 2021), with progress driven by the availability of larger telescopes, the expansion of multifiber spectroscopic capabilities, and, more recently, by large-scale high-resolution spectroscopic surveys, such as, Gaia-ESO (Gilmore et al. 2012), GALactic Archeology with HERMES (GALAH; Martell et al. 2017), and Apache Point Observatory Galactic Evolution Experiment (APOGEE; Majewski et al. 2017). The APOGEE-based Open Cluster Chemical Abundances and Mapping (OCCAM) Survey has produced a comprehensive, uniformly measured data set of infrared spectra for stars in over a hundred open clusters, with the goal of exploiting the advantages of open clusters for constraining key Galactic dynamic and chemical parameters.

Since our previous open cluster chemical abundance gradient study (Donor et al. 2020, OCCAM-IV, hereafter), which was

Original content from this work may be used under the terms of the Creative Commons Attribution 4.0 licence. Any further distribution of this work must maintain attribution to the author(s) and the title of the work, journal citation and DOI.

based on SDSS-IV APOGEE Data Release 16 (DR16; Ahumada et al. 2020), a few new studies of Galactic abundance gradients have been published, most having incorporated the data from OCCAM-IV. For example, Zhang et al. (2021) use a compilation of LAMOST, APOGEE, and other surveys to constrain the metallicity gradient and acquire a high-quality sample of young open clusters. Netopil et al. (2022) also use APOGEE clusters and other studies to characterize the metallicity gradient and its evolution over eight different age bins. Both studies explore the potential effects of radial migration in open clusters, which is possible due to the availability of high-quality kinematic data from the ESA Gaia mission (Gaia Collaboration et al. 2016). The results from the ESA Gaia mission have also significantly improved the ability to refine cluster membership, which is utilized in many studies (e.g., Cantat-Gaudin et al. 2018; Monteiro & Dias 2019; Cantat-Gaudin et al. 2020; Kounkel et al. 2020; Castro-Ginard et al. 2022; Dias et al. 2021).

Galactic abundance gradients are important observable constraints to models of Milky Way chemical evolution, but limitations to these constraints arise from (1) the use of inhomogenous or small data sets, (2) systematic offsets in the abundance results when combining data sets, and (3) uncertainties in cluster ages and distances adopted in the different studies. For example, Donor et al. (2018) found a 40% variation in the gradient slopes when using different distance catalogs but the same set of abundance results. Complications like these have led to a range of values for the metallicity gradients derived from open cluster samples—between roughly -0.05 ± 0.011 dex kpc^{-1} (Reddy et al. 2016; Casamiquela et al. 2019) and -0.1 ± 0.02 dex kpc^{-1} (Jacobson et al. 2016).

Even more recent studies have been able to break down the iron gradient into individual elements to further investigate the processes that enrich the Milky Way; for instance, OCCAM-IV, Spina et al. (2021), Spina et al. (2022), and Sales-Silva et al. (2022), all do so with large open cluster samples.

In this paper, we present the complete OCCAM sample, which is based on the APOGEE results given in the SDSS-IV Data Release 17 (DR17; Blanton et al. 2017; Abdurro'uf et al. 2022), the most recent and final release of data products from Apache Point Observatory Galactic Evolution Experiment 2 (APOGEE-2; Majewski et al. 2017, J. A. Holtzman et al. 2022, in preparation). We analyze Galactic gradient trends in metallicity ([Fe/H]), α elements (O, Mg, Si, S, Ca, Ti), iron-peak elements (V, Cr, Mn, Co, Ni), and other elements (Na, Al, K, Ce) represented in the APOGEE DR17 database, and explore the evolution of these gradients as a function of age. We also calculate the trends with Galactocentric guiding center radius ($R_{\rm guide}$) to investigate the potential biases that may affect the analysis by using the current cluster locations. Finally, we discuss this sample in comparison to other recent literature studies of open clusters.

2. Data

To minimize the systemic offsets inherent to blending multiple data sources, we create a uniform sample for our abundance gradient analyses by pulling the majority of our data from only two sources: SDSS/APOGEE and Gaia. To supplement the SDSS/APOGEE data and provide astrometric and photometric parameters for our analysis we use data from 3, 720, 692 Gaia Early Data Release 3 (EDR3; Gaia Collaboration et al. 2021) stars and radial velocities for 38,667 Gaia stars (Seabroke et al. 2021). We check the offset between Gaia EDR3 RVs and APOGEE DR17 RVs and find the median offset to be roughly -0.14 km s^{-1} with a standard deviation of approximately 2.80 km s^{-1}.

2.1. SDSS/APOGEE DR17

The chemical abundances and radial velocities for the open cluster stars in our sample are from the APOGEE SDSS-IV values in DR17 (Blanton et al. 2017; Abdurro'uf et al. 2022). As previously mentioned, this final data release derives data from the completed collection of high-resolution, near-infrared spectra taken with the APOGEE spectrographs (Wilson et al. 2019) for over 650,000 stars as part of the APOGEE and APOGEE-2 surveys. The SDSS/APOGEE data were taken using two telescopes: the Sloan Foundation telescope at the Apache Point Observatory (New Mexico; Gunn et al. 2006) in the Northern Hemisphere and Du Pont telescope at the Las Campanas Observatory (Chile; Bowen & Vaughan 1973) in the Southern Hemisphere. Observations for APOGEE-2N were concluded in November 2020, while those for APOGEE-2S were concluded in January 2021.

Targeting for the APOGEE survey, including details from this program, are described in Frinchaboy et al. (2010), Zasowski et al. (2013), Zasowski et al. (2017), Beaton et al. (2021), and Santana et al. (2021). APOGEE data are reduced using the APOGEE data reduction pipeline (Nidever et al. 2015) and the ASPCAP data analysis pipeline (García Pérez et al. 2016). The latter produces the detailed abundances of chemical elements (Holtzman et al. 2015, 2018; Jönsson et al. 2020, J. A. Holtzman et al. 2022, in preparation) that are central to the present study.

2.1.1. Pipeline Changes in APOGEE DR17

Some significant changes were made to the APOGEE pipeline for DR17. New synthetic spectral libraries were created using the Synspec code (Hubeny & Lanz 2017; Hubeny et al. 2021) that now allows for the Non-LTE analysis of the elements Na, Mg, K, and Ca using the computations in Osorio et al. (2020). The APOGEE line list used for DR17 is Smith et al. (2021), which updates from Shetrone et al. (2015). While schematic description of the DR17 pipeline is given in Abdurro'uf et al. (2022), further specifics about updates to the APOGEE pipeline will be discussed in J. A. Holtzman et al. (2022, in preparation).

3. Methods

To identify cluster member stars, we employ the analysis described in Donor et al. (2018, 2020), which uses the celestial coordinates (R.A./decl.), proper motion (PM), radial velocity (RV), and metallicity of stellar candidates to sift likely cluster members from nonmembers. All stars designated as cluster members must have RV, PM, and [Fe/H] values within 3σ of the cluster mean. For a more thorough discussion of the probability values, see Section 4.1. As in OCCAM-IV, we also use visual quality checks of both the color–magnitude diagrams (CMDs) and Kiel diagrams ($T_{\rm eff}$ versus log(g)) for the APOGEE stars in each cluster to distinguish between high-quality clusters (with quality flag 1 and 2[22]) and potentially

[22] The quality flag of 2 denotes a cluster used in the calibration sample from Donor et al. (2018).

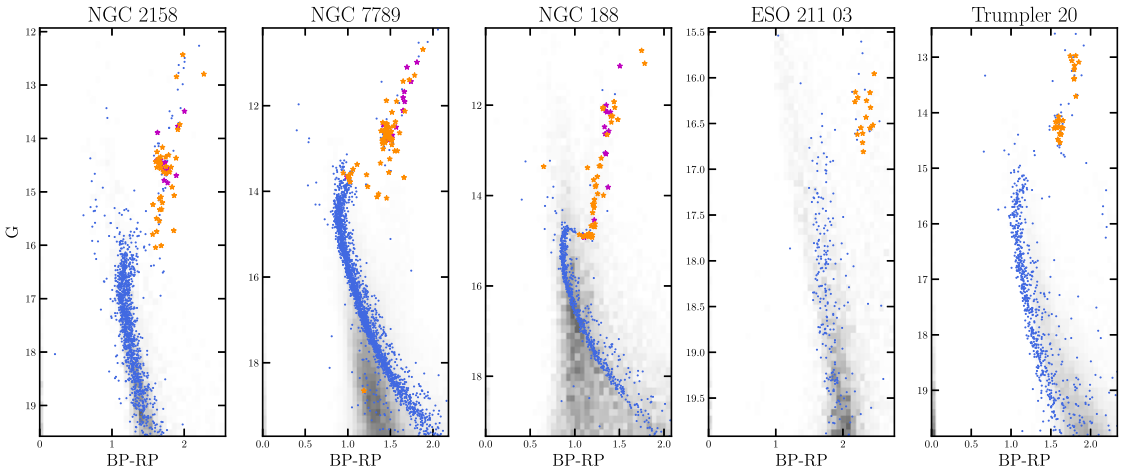

Figure 1. Five example color–magnitude diagrams of open clusters analyzed in this study (Table 1). Stars from Gaia EDR3 within twice the cluster radius, as defined in Cantat-Gaudin et al. (2020), are included; stars identified as PM members and inside the cluster radius are blue. Nonmember stars are shown as a Hess diagram in gray. The OCCAM pipeline-identified APOGEE members from DR16 (Donor et al. 2020) are shown in purple. New DR17 OCCAM pipeline-identified APOGEE member stars are shown as orange stars.

unreliable clusters (with quality flag 0). This procedure is discussed in more detail in OCCAM-IV. As an example of both the CMDs used and the difference between APOGEE DR16 and DR17, we show five example clusters, (all with a quality flag of 1 or 2), in Figure 1. As can be seen, the addition of APOGEE DR17 not only expands the number of stars that are identified to be likely cluster members in previously known clusters, but it also allows new clusters to be added to our sample.

3.1. Methodology Changes from Donor et al. (2020)

The present analysis adopts several changes in methodology from that employed in Donor et al. (2020). In addition to using the latest stellar parameters and abundances from the greatly expanded APOGEE DR17 sample, we also use the latest data from the Gaia Collaboration et al. (2016), EDR3, to take advantage of the extended baseline and expanded astrometric catalog. Additionally, we use the open cluster parameters from Cantat-Gaudin et al. (2020), which exclusively uses Gaia DR2 to compile a catalog that provides uniform measurements of age and distance (among other parameters) for roughly 2000 open clusters. This includes all the open clusters used here for analysis of the Galactic chemical gradients.

Another change in methodology applied to our analysis is the addition of the guiding center radius, $R_{\rm guide}$, which is now used along with galactocentric radius, $R_{\rm GC}$, to compute the Galactic abundance gradients. Methods for the calculation of $R_{\rm guide}$ are further discussed in Section 3.2.[23]

Finally, because more Ce II lines were used in DR17 to determine the abundance of Ce in ASPCAP, the cerium abundance measurements have significantly improved over those in DR16; as a result, we are able to report more precise Galactic trends in cerium here.

[23] For two clusters (FSR 0542 and NGC 2232) that were not initially recovered using the OCCAM-IV pipeline, we implemented a parallax cut for stars greater than twice the reported distance to the cluster (Cantat-Gaudin et al. 2020) and those less than half the distance to the cluster.

3.2. Computing Guiding Center Radii R_{guide}

For each cluster in the sample, we compute its guiding center radius $R_{\rm guide}$ using the circular velocity rotation curve from the best-fitting Milky Way model described in Price-Whelan et al. (2021). The guiding center radius of a given general, eccentric orbit is the radius of a circular orbit with the same angular momentum as the generic orbit. We compute the approximate guiding center radii for the OCCAM clusters by first transforming their heliocentric position and velocity data (sky position, distance, proper motions, and radial velocity) into Galactocentric Cartesian coordinates, assuming solar parameters: for the Sun–Galactic center distance we adopt $R_\odot = 8.275$ kpc (Gravity Collaboration et al. 2021), a solar height above the Galactic midplane of $z_\odot = 20.8$ pc (Bennett & Bovy 2019), and a solar velocity with respect to the Galactic center $\boldsymbol{v}_\odot = (8.42, 250.2, 7.90)$km s^{-1} (Reid & Brunthaler 2004; Drimmel & Poggio 2018; Gravity Collaboration et al. 2018). We then compute the z-component of the angular momentum vector L_z for each cluster in the Galactocentric frame and estimate the guiding center radii as $R_{\rm guide} = L_z/v_c(R)$, where R is the present-day cylindrical radius of each cluster and $v_c(r)$ is the circular velocity curve evaluated at the radius of each cluster.

The use of the guiding center radius of a cluster, rather than its present galactocentric radius, has the advantage of correcting for orbital blurring effects in the metallicity gradients (e.g., Netopil et al. 2022; Spina et al. 2021; Zhang et al. 2021). To illustrate and explore the differences between $R_{\rm guide}$ and $R_{\rm GC}$, we calculate $R_{\rm guide}$, and discuss both radii in Sections 5 and 6.

3.3. Membership Comparison to Cantat-Gaudin et al. (2018)

Cantat-Gaudin et al. (2018) performed a fundamentally different membership analysis than presented here and previously by OCCAM (Donor et al. 2018, 2020). Whereas our analysis relies on kernel convolution and Gaussian fitting to define a rigid boundary for what constitutes "the cluster," Cantat-Gaudin et al. (2018) performed a clustering search in the five-dimensional Gaia phase space (R.A., decl., proper motion, and parallax [ϖ]), requiring no fitting or boundary setting.

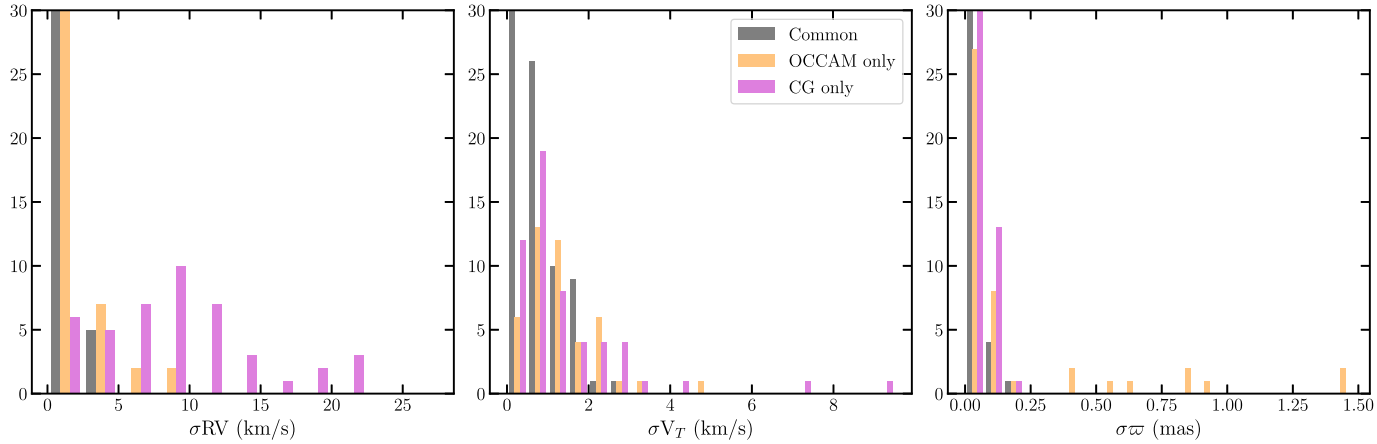

Figure 2. We present the measured standard deviations of three key cluster properties (radial velocity, transverse velocity, and parallax) using three different membership subsamples: (1) includes member stars common to both our OCCAM analysis and Cantat-Gaudin et al. (2018), (2) OCCAM members that are not Cantat-Gaudin et al. (2018) members (OCCAM only), and (3) Cantat-Gaudin et al. (2018) only member stars (CG only). Note that the histogram are artificially cut off at 30 to show relevant detail.

Besides the difference in methodology, the absence of a constraint on parallax in our method, and inclusion of RV and [Fe/H], are noteworthy.

In order to compare the results from the two methods, we divide stars into three categories: common (stars considered cluster members in both the OCCAM and the CG samples), OCCAM only (stars that are included in the present sample but not in Cantat-Gaudin et al. 2018), and CG only (stars rejected from the present sample but included in Cantat-Gaudin et al. 2018). We create a statistic that accentuates differences between these three samples in RV, transverse velocity (V_T, calculated using the cluster distance measured by Cantat-Gaudin et al. (2020)), and parallax (ϖ). To compute this statistic, we first measure the mean cluster value for stars in the common sample ($\bar{x}_{\rm common}$). We then compute the average deviation of the OCCAM only and the CG only samples ($x_{\rm single\ sample}$) from $\bar{x}_{\rm common}$, shown in Equation (1).

$$\sigma_{\rm mod} = \frac{1}{n}\sum(\bar{x}_{\rm common} - x_{\rm singlesample}). \quad (1)$$

In Figure 2, we plot a histogram of RV, V_T, and ϖ with (1) the 1σ standard deviation of the common sample within each cluster in gray, (2) $\sigma_{\rm mod}$ for OCCAM only in orange, and (3) $\sigma_{\rm mod}$ for CG only in purple. There are 92 clusters in our sample where the results of our membership analysis differ from Cantat-Gaudin et al. (2018); we omit the remaining clusters from this analysis as it is designed to show differences. To show relevant detail we artificially cut off each histogram at 30; in all three panels the lowest bin is populated beyond what is shown. Since the common sample is more restrictive than either individual sample it is not surprising that we measure a small standard deviation for the common sample of stars in most clusters. We note the scale difference between the RV and V_T histograms: the first five bins in the V_T plot span 0–2.5 km s^{-1}, which is the size of the first bin in the RV plot.

For the common sample, 67 of 92 clusters for which we measure RV dispersion have measured dispersions below 1 km s^{-1}, and in V_T we find 71 of 92 clusters showing a dispersion below 1 km s^{-1}, in good agreement with typical cluster dispersions (e.g., Cantat-Gaudin & Anders 2020) and despite not explicitly removing binary stars. For ϖ the majority of the OCCAM only clusters show low dispersions, comparable to the common sample and CG only sample, with 83 of 92 clusters having dispersions $<$0.25 mas, despite the fact we have not used ϖ in our selection. For the remaining nine clusters, five are in our low-quality sample. Of the four in our high-quality sample two are very nearby, Melotte 22 (The Pleiades) and Ruprecht 147, so some dispersion in ϖ is expected. The remaining two clusters, FSR 0496 and NGC 7789, each have one star with negative ϖ reported, significantly affecting the measured dispersion.

This analysis shows that despite different selection criteria, the reliability of our sample is comparable to Cantat-Gaudin et al. (2018), where we can compare directly. We find inconsistencies in ϖ in our sample, which is not surprising since ϖ is not accounted for in our analysis. Similarly, we show there is significant RV variation in the Cantat-Gaudin et al. (2018) sample since RV was not accounted for in that analysis. A union of the two samples is straightforward to create using the VAC discussed in Section 4.1. Combining the five-dimensional Gaia phase space with RV and [Fe/H] would produce a purer sample, but in the present work we have chosen to continue using the OCCAM IV membership selection pipeline for consistency.

4. The OCCAM DR17 Sample

Our final sample consists of 150 open clusters with 2061 member stars, out of ∼26,700 stars in the vicinity of a known open cluster considered in this analysis. The final sample of clusters is shown in Figure 3. After a visual CMD inspection (described further in OCCAM-IV), we designate 94 clusters as "high quality." All clusters analyzed are presented in Tables 1 and 2. Where Table 1 includes bulk cluster parameters derived or adopted for this study, and Table 2 includes bulk cluster abundances, which are averaged over the stellar members.

For all Galactic abundance analysis in this study, we choose to use only clusters flagged as high quality and that have distances available from Cantat-Gaudin et al. (2020). Additionally, we also cut out two clusters with an age less than 50 Myr (NGC 7058 and Teutsch 1), due to previous studies suggesting the young star pipeline results from APOGEE may be unreliable (e.g., Kounkel et al. 2018). This results in a sample of 85 clusters.

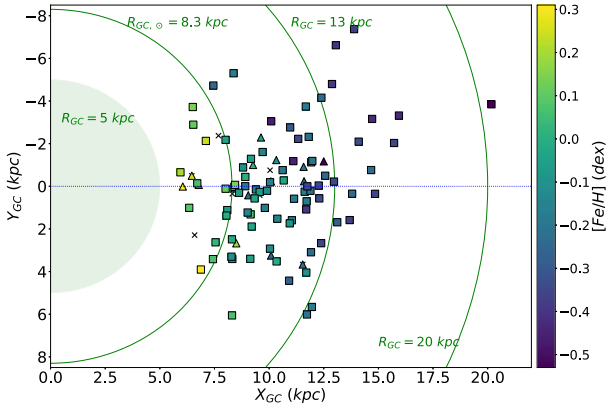

Figure 3. The OCCAM DR17 sample in common with Cantat-Gaudin et al. (2020) plotted in the Galactic plane, color-coded by [Fe/H]. Square points are "high-quality" clusters, triangles are the lower quality clusters, and crosses denote clusters which were in the "high-quality" sample of OCCAM-IV but are now in the "low-quality" sample.

4.1. Data Access—SDSS Value Added Catalog

The VAC consists of two FITS tables. The first, `occam_cluster-DR17.fits`, is a combination of Table 1 and Table 2, providing bulk cluster parameters derived here, PM from Gaia, as well as RVs and average abundances for 16 reliable chemical species available in APOGEE DR17. The second table, `occam_member-DR17.fits`, contains all of the APOGEE stars considered in this analysis (all of the stars that fall within two radii of the cluster center given by Cantat-Gaudin et al. 2020; $2 \times \mathrm{Radius_{CG}}$) and reports the membership probabilities determined by the OCCAM pipelines (for [Fe/H], RV, and PM) as well as the membership probability from Cantat-Gaudin et al. (2020) for convenience. These four probabilities reported reflect how far a given stellar parameter is from the fit cluster mean, where a reported probability of >0.01 is within 3σ of the cluster mean. In practice these fit distributions are fairly tight (see Donor et al. 2018 for a figure set showing distributions for [Fe/H], PM and RV for 19 clusters), therefore a star falling within 3σ[24] of the cluster mean in all three parameter spaces is likely to be a cluster member.

We also note that within the VAC, $R_{\rm GC}$ was calculated with an $R_\odot$ of 8 kpc, whereas for this work, we recalculated $R_{\rm GC}$ with a solar radius of 8.275 kpc to be consistent with Gravity Collaboration et al. (2021).

Table 3 shows all columns available in the occam_member table. The catalog is available from sdss.org.[25]

5. Results

5.1. The Galactic Metallicity Gradient

With the large, uniform sample of open cluster data from APOGEE DR17, we are well positioned to more reliably characterize and report Galactic abundance gradients for 16 chemical species. Figure 4 shows [Fe/H] versus both $R_{\rm guide}$ (top panel) and $R_{\rm GC}$ (bottom panel) for our final sample of 85 open clusters. In both cases we use a two-function gradient, where the gradient is described with two linear functions and where the intersection point of the two lines is also allowed to be a free parameter. We use the fitting procedures described in OCCAM-IV, which uses a maximum likelihood method to fit the data, and the *emcee* python package (Foreman-Mackey et al. 2013) to estimate the fit errors. We assume a 5% error on the distance to each cluster, as (Cantat-Gaudin et al. 2020) did not include distance errors, and these are taken into account in the fitting procedure. We denote the gradient with radius less than the intersection point (hereafter known as the "knee") as the inner gradient and the gradient with radius greater than the knee as the outer gradient. We find an inner gradient of -0.074 ± 0.002 dex kpc^{-1} for $R_{\rm guide}$, and a nearly identical inner gradient of -0.073 ± 0.002 for $R_{\rm GC}$. Meanwhile, the outer gradients for the two cases are: $\mathrm{d[Fe/H]}/R_{\rm guide} = -0.023 \pm 0.003$ dex kpc^{-1} and $\mathrm{d[Fe/H]}/R_{\rm GC} = -0.032 \pm 0.002$ dex kpc^{-1}, with the knee located at 12.2 ± 0.12 kpc and 11.5 ± 0.09 kpc, respectively. For completeness, we also fit the open cluster data from Figure 4 with a single linear function, which is recorded in Table 4, along with the two-function fit and the number of clusters used to calculate both fits (N).

5.2. Galactic Trends for Other Elements

5.2.1. α-Elements—O, Mg, Si, S, Ca, Ti

The Galactic abundance ratio trends for six α-elements (O, Mg, Si, S, Ca, and Ti) over iron versus $R_{\rm guide}$ are shown in Figure 5, these slopes are also reported in Table 5, along with the slopes calculated with $R_{\rm GC}$. We find positive slopes for all studied [α/Fe] abundances but note a significant scatter among the [S/Fe] values and the large uncertainty in the cluster [Ti/Fe] values. There are no significant differences between the best-fit slopes calculated using either $R_{\rm guide}$ or $R_{\rm GC}$.

5.2.2. Iron-Peak Elements—V, Cr, Mn, Co, Ni

In Figure 6, we investigate the Galactic trends versus $R_{\rm guide}$ of the iron-peak element ratios included in DR17 (V, Cr, Mn, Co, and Ni).[26] The gradients for iron-peak elements over iron all show negative, shallow trends (Table 5) with vanadium having the steepest gradient value of all at -0.012 ± 0.008 dex kpc^{-1}, although this is still relatively flat. The cluster values for [V/Fe] also have the largest scatter of the iron-peak elements; however, [Co/Fe] also has three significant outliers: the clusters FSR 0716 ([Co/Fe] $= -0.45$ dex), FSR 1113 ([Co/Fe] $= -0.68$ dex), and Haffner 4 ([Co/Fe] $= -1.01$ dex), which all only have one stellar member in our sample.

5.2.3. Odd-Z Elements—Na, Al, K

The abundance gradients with respect to $R_{\rm guide}$ for the three "odd-z" elements: Na, Al, and K are plotted in Figure 7, and recorded in Table 5 for both $R_{\rm guide}$ and $R_{\rm GC}$. We report similar positive trends for Al and K, but a steep negative gradient for Na. The single one-star outlier for [Na/Fe] corresponds to the open cluster NGC 136.

5.2.4. The Neutron Capture Element Ce

With the availability of reliable abundances for the s-process element Ce, obtained automatically by the ASPCAP pipeline in

[24] In practice we adopt a threshold of 0.01 for all membership probabilities; see Donor et al. (2018, 2020) for further discussion.

[25] The full url is https://www.sdss.org/dr17/data_access/value-added-catalogs/?vac_id=open-cluster-chemical-abundances-and-mapping-catalog.

[26] As discussed in Abdurro'uf et al. (2022) and J. A. Holtzman et al. 2022 (in preparation), the APOGEE DR17 pipeline analysis did not yield sufficiently reliable abundance measurements for the element copper.

Table 1
OCCAM DR17 "High-quality" Sample—Basic Parameters

Cluster name	Qual flag	l deg	b deg	R[a] (′)	Age[a] Gyr	R_{GC}[b] (kpc)	R_{Guide}[b] (kpc)	μ_α[c] (mas yr^{-1})	μ_δ[c] (mas yr^{-1})	RV (km s^{-1})	[Fe/H] (dex)	Num Stars
High-quality Clusters												
Berkeley 2	1	119.7032	−2.3156	3.2	0.59	12.92	13.16	-1.07 ± 0.02	-0.37 ± 0.04	-75.8 ± 2.5	-0.21 ± 0.02	6
Berkeley 17	2	175.6578	−3.6769	8.5	7.24	11.33	11.60	$+2.55 \pm 0.03$	-0.36 ± 0.02	-73.5 ± 0.3	-0.18 ± 0.03	8
Berkeley 18	1	163.5891	5.0296	14.0	4.37	13.48	13.75	$+0.75 \pm 0.03$	-0.09 ± 0.02	-3.0 ± 1.5	-0.37 ± 0.03	30
Berkeley 19	1	176.9168	−3.6100	4.4	2.19	14.55	14.82	$+0.70 \pm 0.01$	-0.30 ± 0.01	$+17.7 \pm 0.1$	-0.36 ± 0.01	1
Berkeley 20	1	203.4853	−17.3763	1.8	4.79	15.99	16.26	$+0.91 \pm 0.01$	-0.27 ± 0.01	$+76.6 \pm 0.2$	-0.43 ± 0.01	1
Berkeley 21	1	186.8174	−2.4901	3.7	2.14	14.39	14.66	$+0.46 \pm 0.03$	-1.02 ± 0.02	$+0.5 \pm 1.1$	-0.23 ± 0.05	8
Berkeley 22	1	199.8736	−8.0708	2.6	2.45	13.95	14.23	$+0.62 \pm 0.03$	-0.40 ± 0.02	$+94.9 \pm 0.8$	-0.33 ± 0.04	6
Berkeley 29	1	197.9472	7.9816	1.7	3.09	20.24	20.51	$+0.11 \pm 0.02$	-1.05 ± 0.02	$+25.3 \pm 0.1$	-0.53 ± 0.02	2
Berkeley 31	1	206.2398	5.1334	3.7	2.82	14.75	15.02	$+0.24 \pm 0.03$	-0.89 ± 0.02	$+58.8 \pm 0.9$	-0.43 ± 0.02	2
Berkeley 33	1	225.4474	−4.5998	3.8	0.23	12.79	13.05	-0.69 ± 0.01	$+1.59 \pm 0.01$	$+77.8 \pm 0.1$	-0.24 ± 0.01	1
.....												

Notes.
[a] Cluster Radius and age from Cantat-Gaudin et al. (2020).
[b] Calculated with distances from Cantat-Gaudin et al. (2020), recomputed to a solar radius of $R_0 = 8.274$ kpc.
[c] μ_α and μ_δ and their 1σ uncertainties are those of the 2D Gaussian fit, as in OCCAMII.

(This table is available in its entirety in machine-readable form.)

Table 2
OCCAM DR17 Sample—Detailed Chemistry

Cluster Name	[Fe/H] (dex)	[O/Fe] (dex)	[Na/Fe] (dex)	[Mg/Fe] (dex)	[Al/Fe] (dex)	[Si/Fe] (dex)	[S/Fe] (dex)	[K/Fe] (dex)
	[Ca/Fe] (dex)	[Ti/Fe] (dex)	[V/Fe] (dex)	[Cr/Fe] (dex)	[Mn/Fe] (dex)	[Co/Fe] (dex)	[Ni/Fe] (dex)	[Ce/Fe] (dex)
High-quality Clusters								
Berkeley 2	-0.21 ± 0.02	-0.01 ± 0.05	$+0.06 \pm 0.66$	-0.02 ± 0.04	$+0.02 \pm 0.03$	-0.01 ± 0.04	$+0.08 \pm 0.11$	$+0.03 \pm 0.08$
	$+0.03 \pm 0.04$	-0.01 ± 0.06	$+0.06 \pm 0.27$	$+0.04 \pm 0.07$	-0.06 ± 0.04	-0.52 ± 0.40	-0.02 ± 0.04	$+0.25 \pm 0.15$
Berkeley 17	-0.18 ± 0.03	$+0.08 \pm 0.02$	$+0.00 \pm 0.07$	$+0.10 \pm 0.02$	$+0.10 \pm 0.03$	$+0.04 \pm 0.02$	$+0.11 \pm 0.05$	$+0.10 \pm 0.04$
	$+0.03 \pm 0.03$	$+0.04 \pm 0.05$	-0.12 ± 0.17	$+0.00 \pm 0.05$	-0.02 ± 0.02	$+0.08 \pm 0.06$	$+0.02 \pm 0.01$	-0.09 ± 0.08
Berkeley 18	-0.37 ± 0.03	$+0.09 \pm 0.06$	$+0.06 \pm 0.18$	$+0.11 \pm 0.02$	$+0.09 \pm 0.05$	$+0.08 \pm 0.04$	$+0.13 \pm 0.08$	$+0.17 \pm 0.13$
	$+0.05 \pm 0.07$	$+0.03 \pm 0.05$	-0.08 ± 0.33	-0.05 ± 0.14	-0.02 ± 0.04	-0.04 ± 0.37	$+0.00 \pm 0.05$	$+0.11 \pm 0.15$
Berkeley 19	-0.36 ± 0.01	$+0.09 \pm 0.02$	$+0.02 \pm 0.08$	$+0.13 \pm 0.02$	$+0.11 \pm 0.03$	$+0.01 \pm 0.02$	$+0.06 \pm 0.06$	$+0.04 \pm 0.05$
	$+0.01 \pm 0.02$	$+0.03 \pm 0.03$	-0.40 ± 0.09	-0.02 ± 0.05	-0.04 ± 0.02	-0.00 ± 0.07	-0.02 ± 0.02	$+0.21 \pm 0.07$
Berkeley 20	-0.43 ± 0.01	$+0.10 \pm 0.01$	$+0.04 \pm 0.07$	$+0.09 \pm 0.01$	$+0.15 \pm 0.02$	$+0.09 \pm 0.02$	$+0.10 \pm 0.05$	$+0.11 \pm 0.05$
	$+0.05 \pm 0.02$	$+0.03 \pm 0.02$	-0.21 ± 0.07	-0.01 ± 0.04	-0.03 ± 0.02	-0.01 ± 0.05	$+0.03 \pm 0.02$	$+0.06 \pm 0.05$
Berkeley 21	-0.23 ± 0.05	-0.00 ± 0.09	$+0.00 \pm 0.14$	$+0.08 \pm 0.04$	$+0.09 \pm 0.04$	-0.04 ± 0.04	$+0.02 \pm 0.08$	-0.01 ± 0.07
	$+0.02 \pm 0.03$	$+0.04 \pm 0.04$	$+0.04 \pm 0.18$	-0.06 ± 0.15	-0.04 ± 0.03	$+0.05 \pm 0.18$	-0.02 ± 0.03	$+0.25 \pm 0.15$
Berkeley 22	-0.33 ± 0.04	$+0.07 \pm 0.03$	$+0.15 \pm 0.11$	$+0.09 \pm 0.02$	$+0.16 \pm 0.08$	$+0.07 \pm 0.02$	$+0.03 \pm 0.17$	$+0.10 \pm 0.11$
	$+0.04 \pm 0.03$	$+0.02 \pm 0.04$	-0.03 ± 0.20	-0.11 ± 0.17	-0.01 ± 0.04	$+0.07 \pm 0.12$	-0.00 ± 0.04	$+0.07 \pm 0.12$
Berkeley 29	-0.53 ± 0.02	$+0.12 \pm 0.01$	$+0.13 \pm 0.07$	$+0.13 \pm 0.02$	$+0.02 \pm 0.03$	$+0.03 \pm 0.02$	$+0.15 \pm 0.06$	$+0.08 \pm 0.05$
	$+0.01 \pm 0.02$	$+0.08 \pm 0.02$	-0.18 ± 0.10	-0.01 ± 0.04	$+0.02 \pm 0.02$	$+0.15 \pm 0.05$	$+0.04 \pm 0.02$	$+0.11 \pm 0.05$
Berkeley 31	-0.43 ± 0.02	$+0.11 \pm 0.02$	$+0.10 \pm 0.08$	$+0.11 \pm 0.02$	$+0.05 \pm 0.08$	$+0.06 \pm 0.02$	$+0.08 \pm 0.06$	$+0.14 \pm 0.05$
	$+0.04 \pm 0.02$	$+0.05 \pm 0.03$	$+0.05 \pm 0.15$	-0.00 ± 0.05	-0.05 ± 0.03	$+0.04 \pm 0.11$	-0.02 ± 0.03	$+0.85 \pm 0.10$
Berkeley 33	-0.24 ± 0.01	$+0.00 \pm 0.01$	$+0.13 \pm 0.06$	$+0.01 \pm 0.01$	$+0.02 \pm 0.02$	-0.01 ± 0.01	$+0.05 \pm 0.04$	-0.04 ± 0.04
	$+0.01 \pm 0.01$	-0.00 ± 0.02	-0.18 ± 0.06	-0.03 ± 0.03	$+0.01 \pm 0.01$	-0.01 ± 0.04	-0.05 ± 0.01	$+0.31 \pm 0.05$
.....								

(This table is available in its entirety in machine-readable form.)

Table 3
A Summary of the Individual Star Data Included in the DR17 OCCAM VAC

Label	Description
CLUSTER	The associated open cluster
2MASS ID	star ID from 2MASS survey
LOCATION_ID[a]	from APOGEE DR16
GLAT	Galactic latitude
GLON	Galactic longitude
FE_H[a]	[Fe/H]
FE_H_ERR[a]	uncertainty in FE_H
VHELIO_AVG[a]	heliocentric radial velocity
VSCATTER[a]	scatter in APOGEE RV measurements
PMRA[b]	proper motion in R.A.
PMDEC[b]	proper motion in decl.
PMRA_ERR[b]	uncertainty in PMRA
PMDEC_ERR[b]	uncertainty in PMDEC
RV_PROB	membership probability based on RV (This study)
FEH_PROB	membership probability based on FE_H (This study)
PM_PROB[c]	membership probability based on PM (This study)
CG_PROB	membership probability from Cantat-Gaudin et al. (2018)

Notes.
[a] Taken directly from APOGEE DR17.
[b] From Gaia EDR3.
[c] Negative values indicate the star is outside the adopted cluster radius, while "2" indicates the star failed our PM membership analysis, but is a member in Cantat-Gaudin et al. (2020).

DR17, we are now able to investigate the abundance gradient of Ce with 69 open clusters in our sample. In Figure 8, we fit [Ce/Fe] abundance versus $R_{\rm guide}$ and find a positive gradient of 0.024 ± 0.006 dex kpc^{-1}. In Table 5, we also report the slope with respect to $R_{\rm GC}$ and find a value of 0.022 ± 0.006 dex kpc^{-1}.

5.3. The Evolution of Galactic Abundance Gradients

5.3.1. Iron

One of the important questions in chemical evolution models is how the Galactic metallicity gradients have evolved over time. Fortunately, the size of our sample lends itself to investigating this question. The open cluster sample studied here can be split into four age bins, divided at 400 Myr, 800 Myr, and 2 Gyr, identical to the bins chosen in OCCAM-IV, although in this study we use the open cluster ages derived in Cantat-Gaudin et al. (2020).

In Figure 9, we plot $R_{\rm guide}$ and $R_{\rm GC}$ versus metallicity for each age bin, showing only clusters with both $R_{\rm GC}$ and $R_{\rm guide} < 16$ kpc. The gradients shown in the figure, however, are calculated with all clusters located within that region (thus the number of clusters changes between the $R_{\rm GC}$ and $R_{\rm guide}$ fits). This gives a sample of 73 clusters for the $R_{\rm guide}$ plots and a sample of 76 clusters for the $R_{\rm GC}$. Two sets of symbols are used in Figure 9: colored triangles denote guiding center radii while galactocentric radii are marked with gray Xs; horizontal bars connect the two radii values for the same cluster. The slope of the gradient calculated with respect to $R_{\rm guide}$ is shown as a solid line, and the slope calculated with $R_{\rm GC}$ is represented as a dashed line. The slopes calculated for each age bin and the number of clusters used for each fit are recorded in Table 4.

As can be seen in Figure 9, the gradients calculated with $R_{\rm GC}$ appear to remain relatively constant between the four age bins, with the first and the fourth bins showing relatively

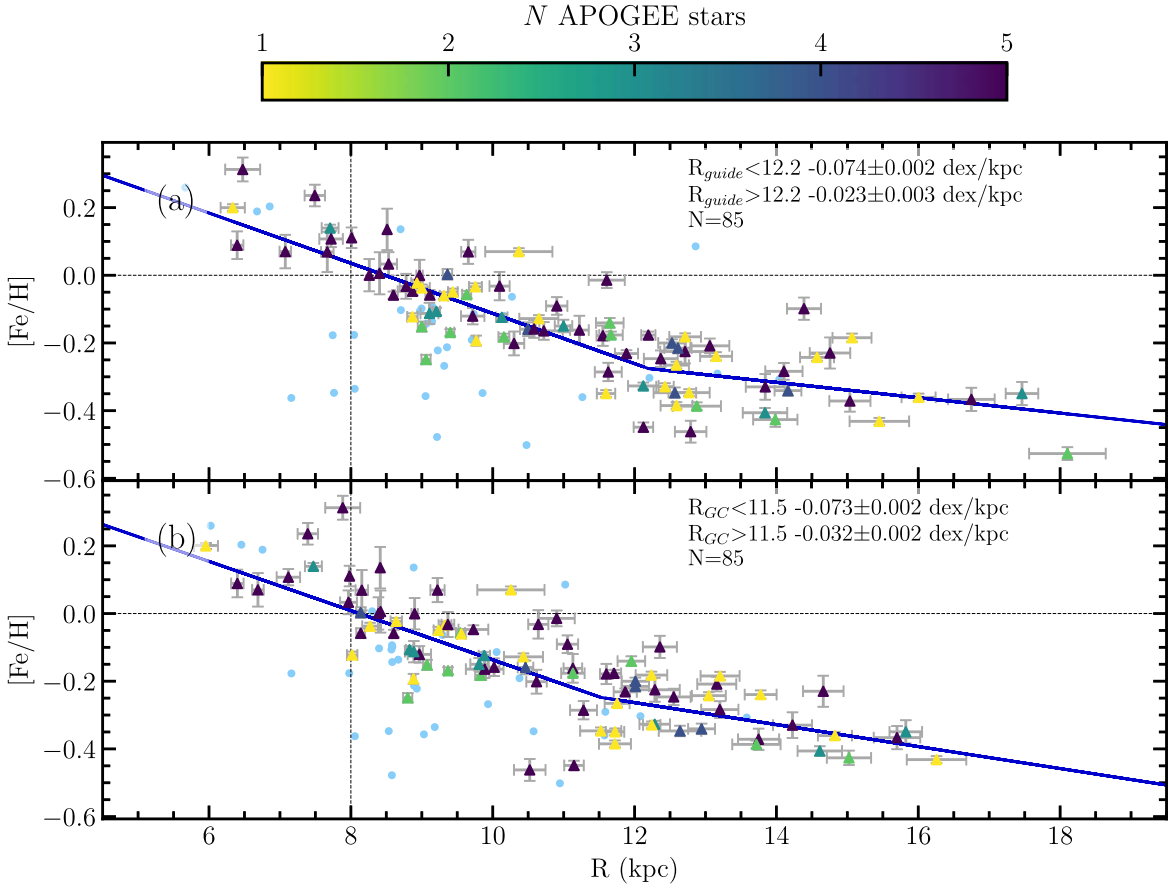

Figure 4. Metallicity ([Fe/H]) gradients from the full high-quality sample mapped as a function of guiding radius ($R_{\rm guide}$; top panel) and current radius ($R_{\rm GC}$; bottom panel), along with a bilinear fit as in Donor et al. (2020). Clusters flagged as potentially unreliable are shown as light blue circles. The color bar indicates the number of OCCAM member stars per cluster, saturating at five.

Table 4
OCCAM DR17 [Fe/H] Gradients

Selection	Type	Gradient (dex kpc^{-1})	Knee (kpc)	N
		d[Fe/H]/d$R_{\rm GC}$		
Inner	Knee	-0.073 ± 0.002	11.5 ± 0.09	85
Outer	Knee	-0.032 ± 0.002	11.5 ± 0.09	85
All	Linear	-0.055 ± 0.001	⋯	85
Age $\leqslant$ 0.4	Linear	-0.052 ± 0.003	⋯	15
0.4 < Age $\leqslant$ 0.8	Linear	-0.059 ± 0.003	⋯	17
0.8 < Age $\leqslant$ 2.0	Linear	-0.059 ± 0.002	⋯	29
Age > 2.0	Linear	-0.052 ± 0.002	⋯	22
		d[Fe/H]/d$R_{\rm Guide}$		
Inner	Knee	-0.074 ± 0.002	12.2 ± 0.12	85
Outer	Knee	-0.023 ± 0.003	12.2 ± 0.12	85
All	Linear	-0.056 ± 0.001	⋯	85
Age $\leqslant$ 0.4	Linear	-0.045 ± 0.003	⋯	15
0.4 < Age $\leqslant$ 0.8	Linear	-0.058 ± 0.003	⋯	17
0.8 < Age $\leqslant$ 2.0	Linear	-0.065 ± 0.002	⋯	27
Age > 2.0	Linear	-0.049 ± 0.002	⋯	22

shallow slopes and the two middle bins having identical slopes. The gradients calculated with $R_{\rm guide}$ seem to show a more constant transition from young to old clusters up until the final age bin, wherein the slope becomes significantly shallower. Additionally, we can see in the last two panels of Figure 9 (i.e,. the two older age bins), that on average the difference between a cluster's $R_{\rm GC}$ and $R_{\rm guide}$ is larger than in the first two age bins (i.e., the younger two age bins). This suggests that as the clusters have had more time to be affected by interactions in the Galaxy, e.g asymmetric drift, their orbits have become more elliptical. Plus, a potential survivor bias in the older cluster samples and/or possible radial migration of clusters could have affected the gradients.

5.3.2. [X/Fe]

To understand the evolution in the radial gradients of elements other than iron, we split the cluster sample into the same four age bins as in Section 6.4.1 and fit each gradient as in Figure 9. Fit parameters for all elements measured both with $R_{\rm guide}$ and with $R_{\rm GC}$ are reported in Table 5. In Figure 10, we also show the slopes (d[X/Fe]/$dR_{\rm guide}$) for all four age bins and each of the 16 elements (where, for iron, we show the abundance ratio [Fe/H]); this figure is comparable to Figure 14 in OCCAM-IV. We note that, as explained in Section 6.4.1, all clusters used in the fit have a radius ($R_{\rm guide}$ or $R_{\rm GC}$) less than 16 kpc.

We find no convincing trends through the four age bins in α elements. While there could be a slight trend in [Mg/Fe], with oldest clusters perhaps showing a steeper slope than younger clusters, the changes between samples are roughly as significant as the uncertainties.

Both [Cr/Fe] and [Ni/Fe] hover around a flat gradient throughout all four age bins, and the gradients of [V/Fe] and

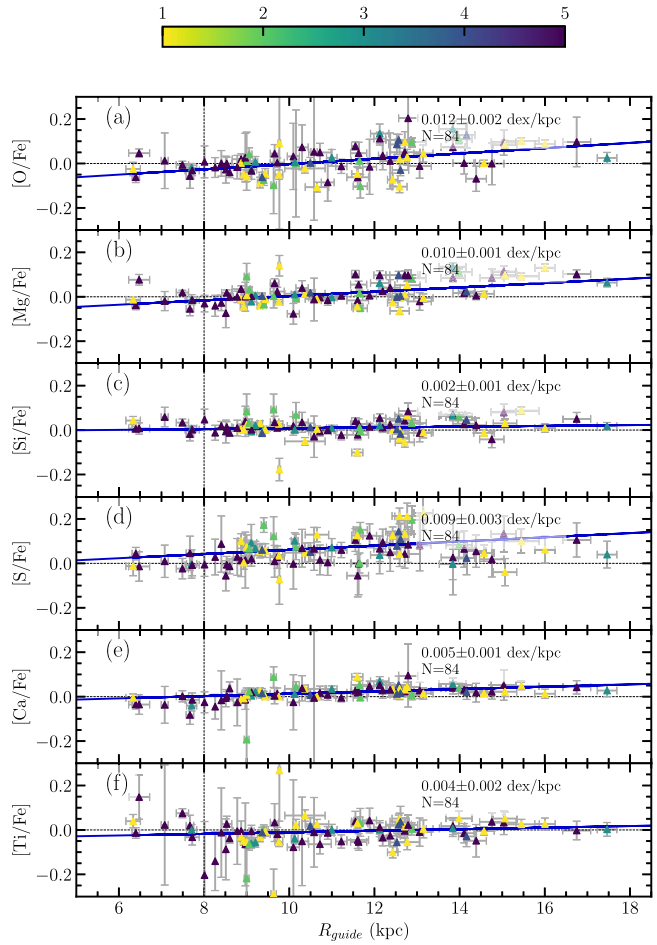

Figure 5. The [X/Fe] vs. $R_{\rm guide}$ trend for the α-elements. As before the color bar indicates number of member stars, saturating at five, and light blue circles represent clusters with high uncertainty in that element.

[Cr/Fe] both have large uncertainties in their measurements, which makes it difficult to determine any evolutionary trends. Additionally, we do not find a significant trend for [Mn/Fe], which breaks with previous APOGEE-based DR16 results presented in OCCAM-IV.

In the odd-Z elements, the gradient for [Na/Fe] seems to have an increasingly negative trend in $R_{\rm guide}$ as clusters get younger, though within the sizeable uncertainty the trend may be less significant. Finally for cerium, the uncertainties in the DR17 measurements are still too large to measure a significant trend over time.

6. Discussion

6.1. Comparison to OCCAM-IV Sample

Between this sample and OCCAM-IV, 111 clusters can be found in both samples, 42 new clusters were added to this sample, and 17 clusters were not recovered, including two "high-quality" clusters: Berkeley 44 and NGC 2355. With updated Gaia EDR3 data, the 2D Gaussian fit to the kernel convolution in proper-motion space was narrower by enough that the APOGEE star now fell further than 3σ from the distribution. For Berkeley 44, the star that was included in OCCAM-IV is now slightly outside of the 2D Gaussian fit to the Gaia EDR3 proper motions. It is also not reported as a member in CG18. For NGC 2355, the star that was included in OCCAM-IV is considered a member in CG18 with a membership probability of 70%, but using updated EDR3 proper motions, the 2D Gaussian fit was more narrow and thus this star was rejected by our pipeline.

Additionally, there were three "high-quality" clusters in OCCAM-IV that were demoted to being flagged as "potentially unreliable" in this sample (SAI 16, BH 211, and Basel 11b). BH 211 failed the visual quality check, and both Basel 11b and SAI 16 had only two potential members with conflicting [Fe/H] values. However, there are seven clusters (Berkeley 91, FSR 0496, King 8, NGC 136, NGC 2202, Saurer 1, and Teutsch 10), which were previously marked "0" or "potentially unreliable" that are now included in the "high-quality" sample due to the addition of new data.

For designated "high-quality" clusters in common between this sample and Donor et al. (2020), a total of 66 clusters, Figure 11 shows the change in [Fe/H] between APOGEE DR16 and DR17. The median change, measured to be -0.020, is well within the measured scatter of 0.033, although this scatter seems to be due mostly to the lowest metallicity clusters ([Fe/H] $\lesssim -0.4$). A visual inspection of the plot suggests that closer to Solar [Fe/H] there may be a real, albeit slight offset from DR16. However, this small offset is easily explainable by the significant changes to the APOGEE pipeline. The single outlier in Figure 11 with a Δ[Fe/H] $= 0.18$ is NGC 752.

Figure 12 shows the change in OCCAM measured cluster abundances for 14 elements from APOGEE DR16 to DR17, plotted as a function of their reported DR17 abundance. These differences are due to pipeline and membership changes. Copper and phosphorus are not included because of unsuccessful measurements in DR17 (Abdurro'uf et al. 2022; J. A. Holtzman et. al 2022, in preparation). Cerium is also not included in Figure 12 because the values reported in DR16 were not considered particularly reliable (Jönsson et al. 2020). The measured median offset is within the measured scatter for all 14 abundances investigated. It is worth commenting on the particularly large scatter, and potential trend, for vanadium and sodium. Vanadium is considered less reliable in both DR16 and DR17; sodium is considered reliable in DR17 but less so in DR16 (Jönsson et al. 2020).

6.2. Comparison to Other Surveys

Spina et al. (2021) use data from GALAH+, APOGEE DR16, and Gaia to compile a list of 226 open clusters, 134 of which have high-quality spectroscopic data for up to 21 elements. Of these clusters 85 are in common with our sample. We compare our sample to the GALAH sample, much like Figure 11, and measure a median offset, (Δ dex, DR17-GALAH) of -0.018 ± 0.046, with two major outliers: King 2 at $+0.18$ and Berkeley 18 at $+0.25$, which both only have one member in the GALAH catalog.

In a recent APOGEE study, Sales-Silva et al. (2022) investigated the abundance gradient for the s-process element, Ce, with a detailed abundance analysis of several Ce II lines from Cunha et al. (2017). They use 218 stellar members of 42 open clusters from the OCCAM-IV sample. In a manner identical to the comparisons above for the OCCAM-IV and GALAH surveys, we compare the [Ce/Fe] abundances for all clusters in common between this sample and the one reported in Sales-Silva et al. (2022). We find not only a systematic shift, but also a subsolar offset for the cerium abundances between the two samples, both between the open clusters and individual

Table 5
OCCAM DR17 Abundance Gradients

Age range R range Gradient	All Clusters All R (dex kpc^{-1})	N	All Clusters[a] $R < 14$ kpc (dex kpc^{-1})	N	Age $\leqslant 0.4$ $R < 16$ kpc (dex kpc^{-1})	N	$0.4 <$ Age $\leqslant 0.8$ $R < 16$ kpc (dex kpc^{-1})	N	$0.8 <$ Age $\leqslant 2.0$ $R < 16$ kpc (dex kpc^{-1})	N	Age > 2.0 $R < 16$ kpc (dex kpc^{-1})	N
Gradients for R_{GC}												
d[O/Fe]/dR_{GC}	$+0.014 \pm 0.002$	84	$+0.015 \pm 0.002$	73	-0.000 ± 0.004	15	$+0.014 \pm 0.007$	17	$+0.009 \pm 0.004$	29	$+0.010 \pm 0.004$	22
d[Mg/Fe]/dR_{GC}	$+0.011 \pm 0.001$	84	$+0.008 \pm 0.001$	73	$+0.001 \pm 0.003$	15	$+0.002 \pm 0.003$	17	$+0.007 \pm 0.002$	29	$+0.012 \pm 0.003$	22
d[Si/Fe]/dR_{GC}	$+0.002 \pm 0.001$	84	$+0.001 \pm 0.001$	73	-0.003 ± 0.003	15	-0.013 ± 0.004	17	$+0.001 \pm 0.002$	29	$+0.002 \pm 0.003$	22
d[S/Fe]/dR_{GC}	$+0.010 \pm 0.003$	84	$+0.017 \pm 0.004$	73	$+0.012 \pm 0.007$	15	$+0.014 \pm 0.011$	17	$+0.010 \pm 0.006$	29	$+0.013 \pm 0.008$	22
d[Ca/Fe]/dR_{GC}	$+0.005 \pm 0.001$	84	$+0.007 \pm 0.002$	73	$+0.006 \pm 0.003$	15	$+0.011 \pm 0.004$	17	$+0.004 \pm 0.003$	29	$+0.005 \pm 0.004$	22
d[Ti/Fe]/dR_{GC}	$+0.004 \pm 0.002$	84	$+0.003 \pm 0.003$	73	$+0.002 \pm 0.005$	15	$+0.015 \pm 0.008$	17	-0.003 ± 0.004	29	$+0.005 \pm 0.006$	22
d[V/Fe]/dR_{GC}	-0.012 ± 0.008	64	$+0.028 \pm 0.011$	58	$+0.037 \pm 0.016$	14	$+0.014 \pm 0.031$	17	$+0.009 \pm 0.017$	29	-0.024 ± 0.020	22
d[Cr/Fe]/dR_{GC}	-0.003 ± 0.004	76	-0.002 ± 0.005	65	$+0.000 \pm 0.008$	15	$+0.006 \pm 0.012$	17	-0.009 ± 0.006	29	-0.008 ± 0.008	22
d[Mn/Fe]/dR_{GC}	-0.007 ± 0.002	82	-0.019 ± 0.002	71	-0.009 ± 0.004	14	$+0.002 \pm 0.004$	17	-0.008 ± 0.003	29	-0.008 ± 0.004	22
d[Co/Fe]/dR_{GC}	-0.006 ± 0.005	62	-0.015 ± 0.007	56	-0.014 ± 0.011	12	-0.040 ± 0.027	14	-0.014 ± 0.011	29	-0.004 ± 0.011	22
d[Ni/Fe]/dR_{GC}	-0.000 ± 0.001	84	-0.003 ± 0.002	73	-0.007 ± 0.003	15	$+0.004 \pm 0.004$	17	-0.003 ± 0.002	29	-0.002 ± 0.003	22
d[Na/Fe]/dR_{GC}	-0.021 ± 0.006	66	-0.031 ± 0.008	56	-0.040 ± 0.014	15	-0.021 ± 0.022	17	-0.025 ± 0.011	29	-0.014 ± 0.013	22
d[Al/Fe]/dR_{GC}	$+0.009 \pm 0.002$	82	$+0.005 \pm 0.003$	71	-0.001 ± 0.005	15	-0.005 ± 0.005	17	$+0.008 \pm 0.004$	29	$+0.008 \pm 0.006$	22
d[K/Fe]/dR_{GC}	$+0.017 \pm 0.003$	80	$+0.017 \pm 0.004$	69	$+0.003 \pm 0.008$	14	$+0.027 \pm 0.011$	17	$+0.015 \pm 0.006$	29	$+0.003 \pm 0.009$	22
d[Ce/Fe]/dR_{GC}	$+0.022 \pm 0.006$	69	$+0.044 \pm 0.009$	60	$+0.034 \pm 0.016$	12	$+0.045 \pm 0.027$	14	$+0.035 \pm 0.012$	29	$+0.056 \pm 0.014$	21
Gradients for R_{guide}												
d[O/Fe]/dR_{guide}	$+0.012 \pm 0.002$	84	$+0.013 \pm 0.002$	73	$+0.002 \pm 0.003$	15	$+0.016 \pm 0.008$	17	$+0.011 \pm 0.005$	27	$+0.008 \pm 0.003$	22
d[Mg/Fe]/dR_{guide}	$+0.010 \pm 0.001$	84	$+0.008 \pm 0.001$	73	$+0.002 \pm 0.003$	15	$+0.005 \pm 0.003$	17	$+0.003 \pm 0.002$	27	$+0.010 \pm 0.002$	22
d[Si/Fe]/dR_{guide}	$+0.002 \pm 0.001$	84	$+0.000 \pm 0.002$	73	-0.002 ± 0.002	15	-0.013 ± 0.004	17	-0.000 ± 0.003	27	$+0.007 \pm 0.003$	22
d[S/Fe]/dR_{guide}	$+0.009 \pm 0.003$	84	$+0.018 \pm 0.004$	73	$+0.009 \pm 0.006$	15	$+0.016 \pm 0.012$	17	$+0.013 \pm 0.007$	27	$+0.013 \pm 0.007$	22
d[Ca/Fe]/dR_{guide}	$+0.005 \pm 0.001$	84	$+0.008 \pm 0.002$	73	$+0.005 \pm 0.003$	15	$+0.009 \pm 0.004$	17	$+0.005 \pm 0.003$	27	$+0.007 \pm 0.003$	22
d[Ti/Fe]/dR_{guide}	$+0.004 \pm 0.002$	84	$+0.002 \pm 0.003$	73	$+0.003 \pm 0.004$	15	$+0.014 \pm 0.008$	17	-0.006 ± 0.005	27	$+0.004 \pm 0.006$	22
d[V/Fe]/dR_{guide}	-0.011 ± 0.008	64	$+0.038 \pm 0.011$	58	$+0.024 \pm 0.014$	14	$+0.037 \pm 0.031$	17	$+0.013 \pm 0.018$	27	-0.016 ± 0.018	22
d[Cr/Fe]/dR_{guide}	-0.003 ± 0.003	76	-0.001 ± 0.005	65	-0.000 ± 0.007	15	$+0.008 \pm 0.013$	17	-0.006 ± 0.008	27	-0.007 ± 0.008	22
d[Mn/Fe]/dR_{guide}	-0.007 ± 0.002	82	-0.011 ± 0.002	71	-0.007 ± 0.003	14	$+0.002 \pm 0.005$	17	-0.012 ± 0.003	27	-0.008 ± 0.004	22
d[Co/Fe]/dR_{guide}	-0.007 ± 0.005	62	-0.023 ± 0.007	56	-0.010 ± 0.009	12	-0.069 ± 0.033	14	-0.038 ± 0.014	27	-0.008 ± 0.009	22
d[Ni/Fe]/dR_{guide}	-0.001 ± 0.001	84	-0.004 ± 0.002	73	-0.006 ± 0.002	15	$+0.003 \pm 0.004$	17	-0.006 ± 0.003	27	$+0.001 \pm 0.003$	22
d[Na/Fe]/dR_{guide}	-0.020 ± 0.006	66	-0.035 ± 0.008	56	-0.030 ± 0.012	15	-0.022 ± 0.022	17	-0.032 ± 0.013	27	-0.013 ± 0.010	22
d[Al/Fe]/dR_{guide}	$+0.009 \pm 0.002$	82	$+0.005 \pm 0.003$	71	$+0.001 \pm 0.004$	15	-0.001 ± 0.006	17	$+0.008 \pm 0.004$	27	$+0.008 \pm 0.005$	22
d[K/Fe]/dR_{guide}	$+0.016 \pm 0.003$	80	$+0.017 \pm 0.004$	69	$+0.004 \pm 0.007$	14	$+0.029 \pm 0.011$	17	$+0.014 \pm 0.008$	27	$+0.007 \pm 0.008$	22
d[Ce/Fe]/dR_{guide}	$+0.024 \pm 0.006$	69	$+0.051 \pm 0.010$	60	$+0.029 \pm 0.013$	12	$+0.047 \pm 0.027$	14	$+0.050 \pm 0.014$	27	$+0.028 \pm 0.012$	21

Note.
[a] While not explicitly discussed in text we report the gradient cut at 14 kpc in order to easily compare to previous work.

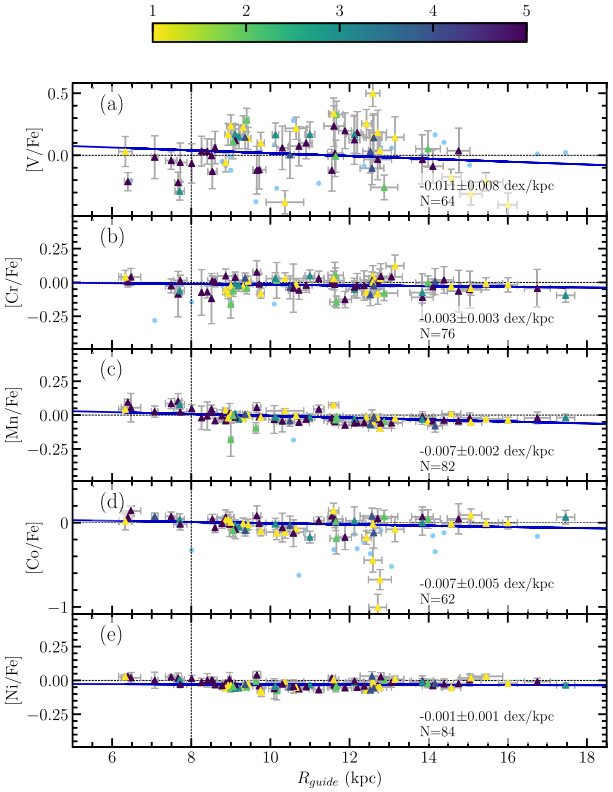

Figure 6. Same as Figure 5, but for the iron-peak elements.

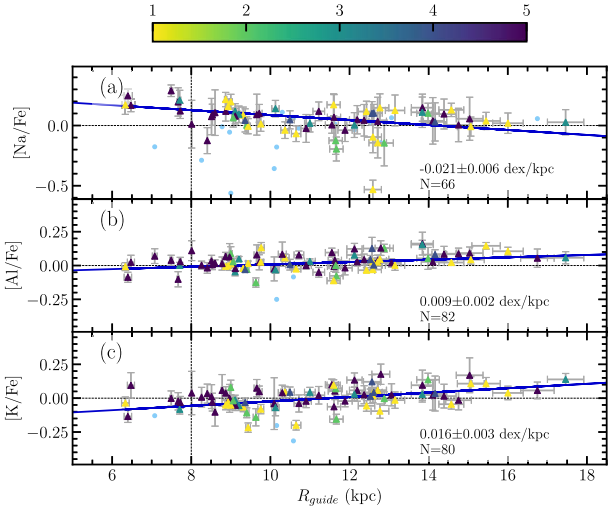

Figure 7. Same as Figure 5 but for the "odd-z" elements.

stellar abundances. This shift may be due to BACCHUS, as used by Sales-Silva et al. (2022), not properly excluding CNO blending from targeted lines. We additionally compared to the high-resolution optical follow-up analysis of APOGEE stars in clusters from O'Connell (2017) and J. E. O'Connell et al. (2022, in preparation), which gives similar results to Sales-Silva et al. (2022). Given the possible uncertainties with cerium, we present the DR17 OCCAM results here, but suggest further work is needed to settle this discrepancy.

6.3. Comparison of Galactic Abundance Trends

In order to evaluate our reported gradients, we compare them against previous studies in this section. For our metallicity

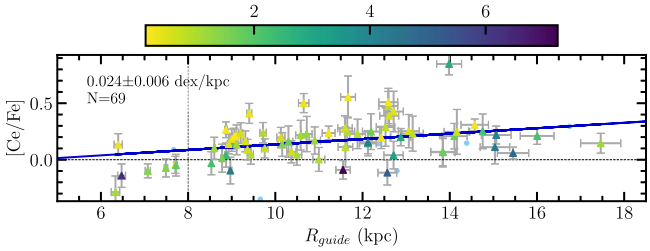

Figure 8. The Galactic abundance trend for cerium. The points are colored by their age in Gyr.

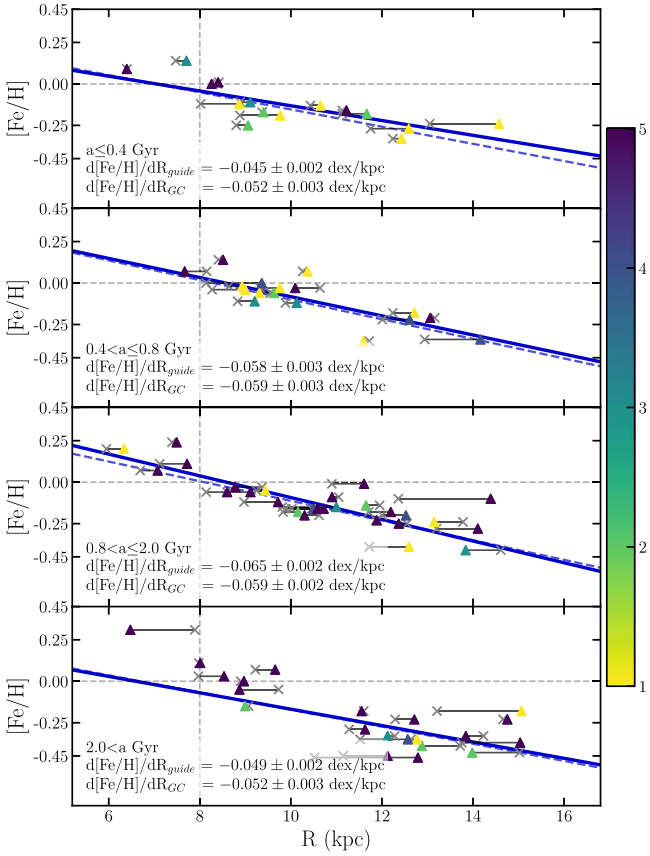

Figure 9. The Galactic [Fe/H] vs. radius trend in four age bins. Gray "X"s represent the R_{GC} of the cluster, while the colored triangles show R_{guide}, both of these values are connected with a thin gray line for each cluster. The solid line shows the [Fe/H] vs. R_{guide} trend, and the dashed line is the trend for R_{GC}.

gradient comparisons, we use our full sample of open clusters. However, for the individual abundance gradient comparisons in Sections 6.3.2–6.3.5, we use gradients with a cut in radius at 14 kpc (Table 5), as the other studies do not have significant clusters beyond 14 kpc.

6.3.1. Galactic Metallicity Gradient

Our derived metallicity trend—namely an inner gradient of -0.073 ± 0.002 dex kpc^{-1}, outer gradient of -0.032 ± 0.002 dex kpc^{-1}, and break at 11.5 kpc for R_{GC}—shows a very similar inner gradient to that reported in OCCAM-IV (theirs being -0.068 ± 0.004 dex kpc^{-1}). However, our measured outer gradient is significantly steeper than the OCCAM-IV value of -0.009 ± 0.011 dex kpc^{-1}, and the knee measured here is farther inwards than theirs (13.9kpc). These discrepancies are

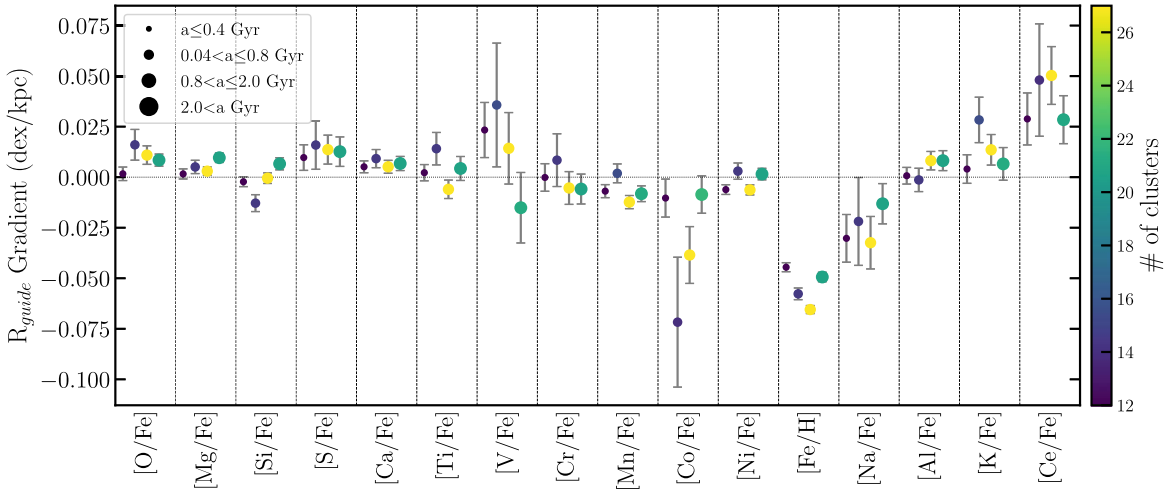

Figure 10. The slopes of each elemental gradient in four age bins (as in Figure 9), for $R_{\rm guide}$. Point size increases with age, and the color indicates the number of clusters included in the gradient measurement.

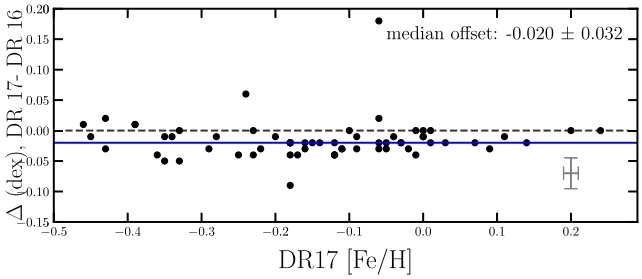

Figure 11. Comparing the DR17 and DR16 [Fe/H] abundances. The measured median offset is shown as a solid blue line. A characteristic error bar is shown for reference.

most likely due to poor coverage of clusters at $R_{\rm GC} > 14$ kpcs in the OCCAM-IV sample, as noted in that study.

The Netopil et al. (2022) study finds an overall linear gradient of -0.058 ± 0.004 dex kpc^{-1}, which is only slightly steeper than our measured single linear slope of -0.056 ± 0.001 dex kpc^{-1}. They also measure an inner disk ($R_{\rm GC} < 12$ kpc) gradient of -0.058 ± 0.005 dex kpc^{-1}, which is significantly shallower than our reported values.

Similarly, Spina et al. (2021) measure a linear trend for their sample of open clusters of $d[{\rm Fe/H}]/R_{\rm GC} = -0.076 \pm 0.009$ dex kpc^{-1} and $d[{\rm Fe/H}]/R_{\rm guide} = -0.073 \pm 0.008$ dex kpc^{-1}, for clusters between roughly $6 \leqslant R \leqslant 14$ kpc. Both of these slopes are consistent with the present inner gradients of -0.073 ± 0.002 dex kpc^{-1} and -0.074 ± 0.002 dex kpc^{-1}, respectively; however with the additional clusters beyond ∼14 kpc in this sample, we find a much shallower linear gradient in both $R_{\rm GC}$ and $R_{\rm guide}$.

6.3.2. α–Elements—O, Mg, Si, S, Ca, Ti

Our results for the $\alpha-$elements are largely in agreement with those of OCCAM-IV, with an exception for the gradient in [Ca/Fe] which, in the DR17 sample is significantly flatter (0.007 ± 0.002 dex kpc^{-1}) than was reported with the DR16 sample (0.012 ± 0.001 dex kpc^{-1}). Our gradients for silicon and titanium ($d[{\rm Si/Fe}]/dR_{\rm GC} = +0.001 \pm 0.001$ dex kpc^{-1} and $d[{\rm Ti/Fe}]/dR_{\rm GC} = 0.003 \pm 0.003$ dex kpc^{-1}) are also slightly steeper than those reported in OCCAM-IV ($d[{\rm Si/Fe}]/dR_{\rm GC} = -0.001 \pm 0.001$ dex kpc^{-1} and $d[{\rm Ti/Fe}]/dR_{\rm GC} = 0.000 \pm 0.002$ dex kpc^{-1}), but they are nearly the same within the measured uncertainties.

Spina et al. (2021) find a comparatively steep gradient in [O/Fe] versus $R_{\rm guide}$ of 0.032 ± 0.01 dex kpc^{-1}, significantly different from the present measurement of $+0.013 \pm 0.002$ dex kpc^{-1}. The steep [O/Fe] versus $R_{\rm guide}$ gradient stands out from other gradients in α elements in Spina et al. (2021), and the reported uncertainty, is larger as well. While Casamiquela et al. (2019) reports a steep gradient for [Si/Fe] versus $R_{\rm GC}$ of 0.022 ± 0.007, similar to the steep [O/Fe] versus $R_{\rm GC}$ gradient from Spina et al. (2021), steep gradients in α elements are not commonly reported. Indeed, gradients measured for other α elements (Mg, Si, Ca, and Ti) by Spina et al. (2021) are nearly flat. This also stands in some contrast to the present work as we consistently measure mildly positive gradients in the same elements. This general trend of mildly positive gradients in α elements is consistent with OCCAM-IV, and previous literature (e.g., Carrera & Pancino 2011; Yong et al. 2012; Reddy et al. 2016) as discussed in OCCAM-IV.

6.3.3. Iron-Peak Elements—V, Cr, Mn, Co, Ni

The gradients we reported in Table 5 for nickel, cobalt, manganese, and vanadium are in good agreement with those in OCCAM-IV. However, the gradient for [Cr/Fe] measured here (-0.002 ± 0.005 dex kpc^{-1}) does deviate slightly from that measured in OCCAM-IV (0.010 ± 0.004 dex kpc^{-1}). This seems to be due to minute changes in abundances, particularly in those clusters at radii less than ∼7 kpc, which affects the gradient and accounts for the discrepancy.

The slopes measured for [Cr/Fe] (-0.003 ± 0.004 dex kpc^{-1}) is consistent with the compiled gradient from the Open Cluster Chemical Abundances of the Spanish Observatories survey (OCCASO; Casamiquela et al. 2019), -0.005 ± 0.003 dex kpc^{-1}. However, the measured slope for [V/Fe], 0.028 ± 0.011 dex kpc^{-1}, is inconsistent with that measured in OCCASO. This discrepancy can easily be accounted for due to the large scatter present in both gradients. Both this study and the OCCASO study also measure a very flat gradient for [Ni/Fe], however the final values (-0.003 ± 0.002 dex kpc^{-1} in this sample and 0.002 ± 0.001 dex kpc^{-1} in the OCCASO sample) are just outside of the uncertainties.

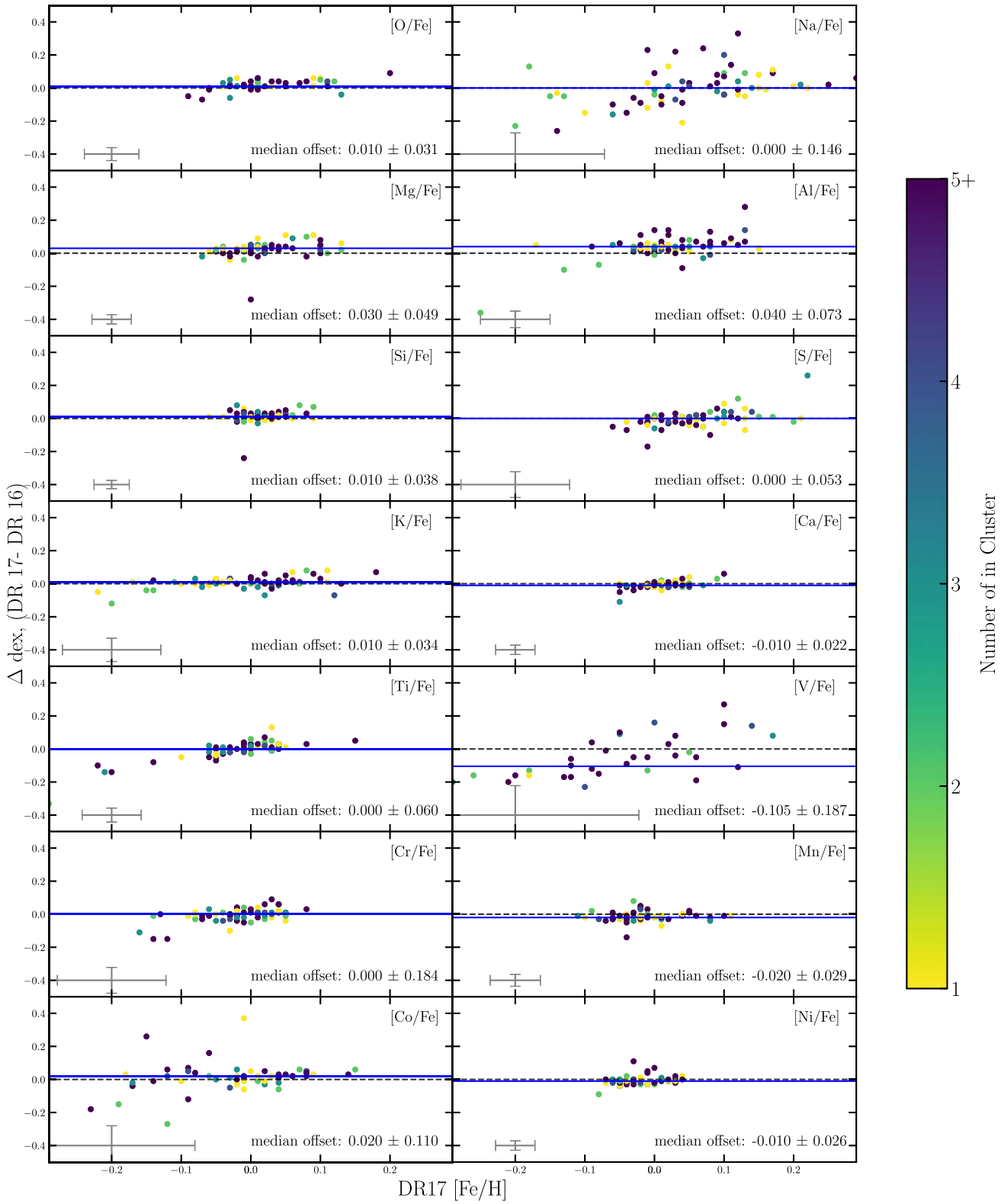

Figure 12. A comparison of DR17 vs. DR16 for each chemical element in our study. Characteristic error bars, calculated identically to those in Figure 11, are indicated in each panel. Median offsets between the DR17 and DR16 values for clusters in common are shown by a blue line, while data points are colored by the number of stars in the DR17 cluster.

Finally, the slope from this sample for [Mn/Fe] (-0.011 ± 0.002 dex kpc^{-1}) is consistent with that reported in Spina et al. (2021; -0.012 ± 0.004 dex kpc^{-1}). However, the slope reported in this study for the [Ni/Fe] gradient (-0.004 ± 0.002 dex kpc^{-1}) is significantly shallower and for the [Co/Fe] gradient (-0.023 ± 0.007 dex kpc^{-1}) is significantly steeper than the gradients

reported in Spina et al. (2021; -0.022 ± 0.006 dex kpc^{-1} and -0.007 ± 0.007 dex kpc^{-1}, respectively).

6.3.4. Odd-Z Elements—Na, Al, K

The gradient calculated for [Na/Fe] and [K/Fe] (-0.031 ± 0.006 dex kpc^{-1} and 0.017 ± 0.003 dex kpc^{-1}) is consistent with those reported in OCCAM-IV. However, the slope of the [Al/Fe] gradient, 0.005 ± 0.003 dex kpc^{-1}, is significantly shallower than the slope reported in OCCAM-IV (0.018 ± 0.002 dex kpc^{-1}) and entirely inconsistent with the value reported in Spina et al. (2021; -0.013 ± 0.007 dex kpc^{-1}). Additionally, the measured gradient, d[Na/Fe]$/dR_{\rm guide} = -0.035 \pm 0.008$ dex kpc^{-1}, is inconsistent with that measured in Spina et al. (2021; -0.008 ± 0.010 dex kpc^{-1}). However, we note that this sample has a greater number of clusters at larger distances than the Spina et al. (2021) sample, which flattens the gradient. Additionally, the gradient measured by Spina et al. (2021) seems to be dominated by a few [Al/Fe] enhanced clusters in the inner galaxy, which we do not see in our sample. Finally, the OCCAM-IV [Al/Fe] gradient includes a few single-star clusters at low [Al/Fe], which resulted in a steeper measured gradient.

6.3.5. The Neutron Capture Element Ce

Shown in Figure 8, and reported in Table 5, we find a positive cerium abundance gradient of d[Ce/Fe]$/dR_{\rm guide} = 0.024 \pm 0.006$ dex kpc^{-1} and d[Ce/Fe]$/dR_{\rm GC} = 0.022 \pm 0.006$ dex kpc^{-1}. Comparing these slopes to the gradients calculated in Sales-Silva et al. (2022), their value for d[Ce/Fe]$/dR_{\rm GC}$ of 0.014 ± 0.007 dex kpc^{-1} is shallower than the value found here, though much of this discrepancy may be explained by the measurement differences as described in Section 6.2.

6.4. Evolution of Galactic Abundance Gradients

6.4.1. Iron

One of the key goals of the OCCAM project is to explore the evolution of abundance gradients in the Milky Way. To this end, we find significant evolution in the d[Fe/H]$/dR$ gradients as presented in Section 5.1. This same trend has also been shown in OCCAM-IV, Spina et al. (2021), Sales-Silva et al. (2022), Netopil et al. (2022), and Zhang et al. (2021).

Netopil et al. (2022) explored the evolution of the [Fe/H] gradient by compiling a sample of 136 open clusters from various studies, including 75 clusters with data from APOGEE DR16, 70 of which are in common with this sample. The details of the compilation are recorded in both Netopil et al. (2016) and Netopil et al. (2022). The latter used this sample to investigate radial migration in open clusters and also measure the age–metallicity gradient with eight overlapping age bins. These age bins span from the youngest clusters (age < 0.4 Gyr) to clusters with age $\geqslant 5.2$ Gyr.

To better compare our results to that of Netopil et al. (2022), we divided our sample into their age bins (Figure 13); however, to populate the oldest age bin with more than 10 clusters, we modified the oldest age bin from the Netopil et al. (2022) limits $3.0 \geqslant$ age $\geqslant 5.2$ Gyr to instead include all clusters with age $\geqslant 3.0$ Gyr.

Comparing to Table 6 in Netopil et al. (2022), the gradients we measure in Figure 13 are in good agreement for nearly every age bin, with measurements in six of the eight samples agreeing well within the reported uncertainties. However, in the first age bin, the discrepancy between the two gradients is $\sim$0.004 dex kpc^{-1}; and for the final age bin the discrepancy is $\sim$0.008 dex kpc^{-1}. We note that the final age bin is largely affected by two relatively metal-poor clusters at $R_{\rm guide} \simeq 12$ kpc, NGC 2243 and Trumpler 5.

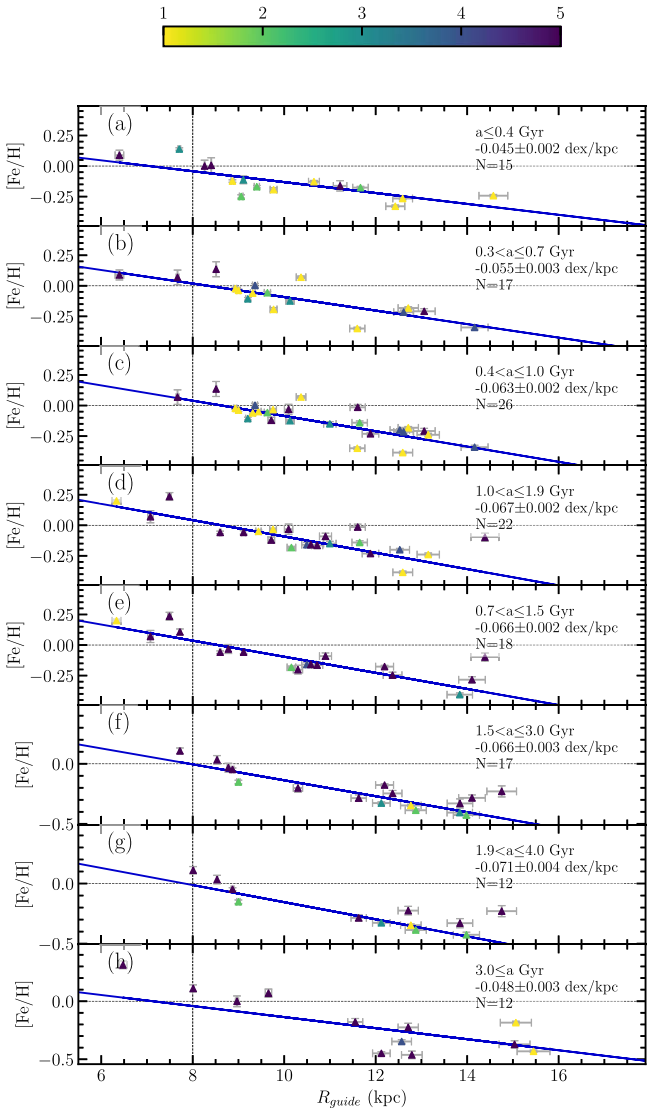

Figure 13. The age slopes measured if the age bins used in (Netopil et al. 2022) are adopted.

Finally, we compare our [Fe/H] evolution results to the thin-disk chemical evolution model of Chiappini (2009) and the chemo-dynamical simulation of (Minchev et al. 2013, 2014; MCM in Figure 14), using the same age bins as Figure 9. In the youngest three age bins we notice good agreement for both $R_{\rm GC}$ and $R_{\rm guide}$ trends. The third age bin also shows decent agreement, though there may be a slight offset between the $R_{\rm guide}$ cluster sample and the model results. In the final age bin, both the $R_{\rm GC}$ and $R_{\rm guide}$ cluster sample have a noticeable offset from the models. This could potentially suggest either a real effect that would require a change to the models or that the older open clusters are possibly a biased sample due to which clusters survive to older ages and/or that these old clusters may have undergone migration and migrated outward during their

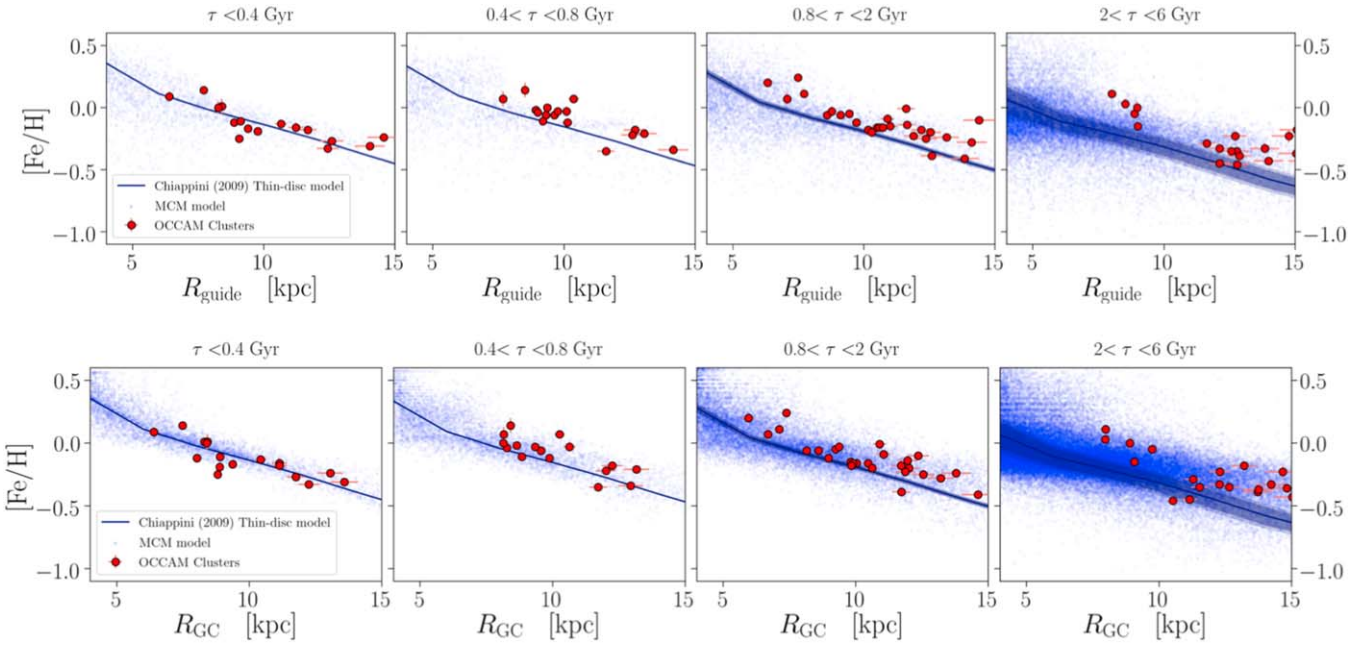

Figure 14. The open cluster sample from this study (red dots) overlaid on the models of Chiappini (2009; the blue line) and Minchev et al. (2013, 2014; blue dots). The plots are split into the same age bins used in Figure 9.

lifetimes (whereas clusters that moved inward in the Milky Way are more likely to be disrupted).

6.4.2. [X/Fe]

The evolution of abundance gradients for elements besides iron were explored in Section 5.2. A similar analysis in OCCAM-IV indicated no convincing trends in α elements with time. As in OCCAM-IV, it could be argued that there is a slight trend for [Mg/Fe], with older clusters perhaps showing generally steeper slopes than the younger clusters, but also as in OCCAM-IV the changes between samples are roughly as significant as the uncertainties.

There is very little evolution found for [Cr/Fe] and [Ni/Fe], which is consistent with the OCCAM-IV results. As is the case here, OCCAM-IV found significant uncertainty in the [Cr/Fe] measurements, but the [Ni/Fe] gradients were fairly well determined. OCCAM-IV found a significant trend for [Mn/Fe] with the gradient becoming more negative for younger cluster populations. With the new DR17 data, this trend is no longer present; indeed the new APOGEE results seem to indicate that the younger samples have less negative gradients.

Finally, while we do seem to see an increasingly negative trend in $\mathrm{d[Na/Fe]/d}R_{\mathrm{guide}}$ as clusters get younger, the uncertainties in the gradients are large. This is roughly consistent with the slopes calculated in OCCAM-IV, though they found a flatter trend with a significantly steeper slope in the oldest age bin that we do not see here.

7. Conclusions

We present the final APOGEE-2 DR17 OCCAM sample, which consists of 150 open clusters, and 94 that we designate as "high quality". To gain insights into the chemical enrichment history of the Milky Way, we use the high-quality sample to measure Galactic abundance gradients in 16 chemical elements and investigate their evolution over four age bins. With clusters spanning roughly 6.0–18 kpc, we measure a two-function Galactic radial metallicity trend, with -0.073 ± 0.002 dex kpc^{-1} for the inner slope, -0.032 ± 0.002 dex kpc^{-1} for the outer slope, and a knee located at 11.5 kpc. In order to account for blurring effects in the clusters orbits, we also calculate the guiding center radii, R_{guide}, of each cluster. By using R_{guide} as the independent variable, we find an inner slope of -0.074 ± 0.002 dex kpc^{-1}, an outer slope of -0.023 ± 0.003 dex kpc^{-1}, and a knee at 12.2 kpc.

The Galactic radial gradients for the 15 elements measured in this survey are in good agreement with other recent studies (e.g., Reddy et al. 2016; Casamiquela et al. 2019; Donor et al. 2020; Spina et al. 2021). In this work, we find significant (3σ or greater) trends in 9 of the 15 elements, including four of the $\alpha-$elements (O, Mg, S, Ca), all of the odd-Z elements (Na, Al, K), and cerium. We do not find significant gradients in the iron-peak elements, except manganese.

We explore the variation in the trends for all elements throughout time, by splitting the open cluster sample into four age bin. We find no significant evolution compared with solar ratios, besides two elements (V and Na), which have large uncertainty in their measurements. This lack of age variation in the gradients points to well-mixed enrichment through the age range covered (10 Myr–9 Gyr), which implies that chemical tagging distinct *age* populations may be difficult with these elements, but could be improved with the inclusion of C and N (e.g., Casali et al. 2019; Spoo et al. 2022) for distinct stellar evolutionary phases.

We compare this DR17-based sample to OCCAM-IV and the GALAH sample from Spina et al. (2021) and find no significant differences between the abundances in either case. Additionally, we compare against the cerium abundances derived in Sales-Silva et al. (2022) and find an abundance correlated offset for subsolar cerium abundances between the BACCHUS analyses and the DR17 ASPCAP-derived values.

We find general agreement in the first three age bins when we compare to the chemo-dynamical models of Chiappini (2009) and Minchev et al. (2013, 2014); however, in the final age bin we do find an offset between the cluster sample and the

models. This could be explained by either an offset in the models or, possibly, by a potential survivor bias in the older open cluster sample.

Also, we note that APOGEE DR17 is able to measure Galactic trends for many of the CHNOPS elements, e.g., C,N, O, and S, which are important in the astrobiological study of the Galactic habitable zone. In this work, we present the gradients for oxygen and sulfur. The gradients for carbon and nitrogen are not presented here due to stellar evolutionary effects that change stellar surface chemistry due to the dredge up; however, these elements and their correlations with age are explored in Spoo et al. (2022).

We would like to greatly thank Friedrich Anders for helping with the creation of figures used for comparison to the Chiappini model.

N.M., J.D., P.M.F., T.S., and A.E.R. acknowledge support for this research from the National Science Foundation (AST-1715662). P.M.F. and A.P.W. acknowledge this work was performed at the Aspen Center for Physics, which is supported by National Science Foundation grant PHY-1607611. D.A.G. H. acknowledges support from the State Research Agency (AEI) of the Spanish Ministry of Science, Innovation and Universities (MCIU) and the European Regional Development Fund (FEDER) under grant AYA2017-88254-P. D.G. gratefully acknowledge support from the Chilean Centro de Excelencia en Astrofísica and financial support from the Dirección de Investigación y Desarrollo de la Universidad de La Serena through the Programa de Incentivo a la Investigación de Académicos (PIA-DIDULS). D.M. is supported by ANID BASAL project FB210003. H.J. acknowledges support from the Crafoord Foundation, Stiftelsen Olle Engkvist Byggmästare, and Ruth och Nils-Erik Stenbäcks stiftelse. A.R.L. acknowledges financial support provided in Chile by Comisión Nacional de Investigación Científica y Tecnológica (CONICYT) through the FONDECYT project 1170476 and by the QUIMAL project 130001.

Funding for the Sloan Digital Sky Survey IV has been provided by the Alfred P. Sloan Foundation, the U.S. Department of Energy Office of Science, and the Participating Institutions.

SDSS-IV acknowledges support and resources from the Center for High Performance Computing at the University of Utah. The SDSS website is www.sdss.org.

SDSS-IV is managed by the Astrophysical Research Consortium for the Participating Institutions of the SDSS Collaboration including the Brazilian Participation Group, the Carnegie Institution for Science, Carnegie Mellon University, Center for Astrophysics |Harvard & Smithsonian, the Chilean Participation Group, the French Participation Group, Instituto de Astrofísica de Canarias, The Johns Hopkins University, Kavli Institute for the Physics and Mathematics of the Universe (IPMU)/University of Tokyo, the Korean Participation Group, Lawrence Berkeley National Laboratory, Leibniz Institut für Astrophysik Potsdam (AIP), Max-Planck-Institut für Astronomie (MPIA Heidelberg), Max-Planck-Institut für Astrophysik (MPA Garching), Max-Planck-Institut für Extraterrestrische Physik (MPE), National Astronomical Observatories of China, New Mexico State University, New York University, University of Notre Dame, Observatário Nacional/MCTI, The Ohio State University, Pennsylvania State University, Shanghai Astronomical Observatory, United Kingdom Participation Group, Universidad Nacional Autónoma de México, University of Arizona, University of Colorado Boulder, University of Oxford, University of Portsmouth, University of Utah, University of Virginia, University of Washington, University of Wisconsin, Vanderbilt University, and Yale University.

This work has made use of data from the European Space Agency (ESA) mission Gaia (https://www.cosmos.esa.int/gaia), processed by the Gaia Data Processing and Analysis Consortium (DPAC; https://www.cosmos.esa.int/web/gaia/dpac/consortium). Funding for the DPAC has been provided by national institutions, in particular the institutions participating in the Gaia Multilateral Agreement.

This research made use of Astropy, a community-developed core Python package for Astronomy (Astropy Collaboration, 2018).

Facilities: Du Pont (APOGEE), Sloan (APOGEE), Spitzer, WISE, 2MASS, Gaia.

Software: Astropy.

ORCID iDs

Natalie Myers https://orcid.org/0000-0001-9738-4829
Taylor Spoo https://orcid.org/0000-0003-4019-5167
Peter M. Frinchaboy https://orcid.org/0000-0002-0740-8346
Katia Cunha https://orcid.org/0000-0001-6476-0576
Adrian M. Price-Whelan https://orcid.org/0000-0003-0872-7098
Steven R. Majewski https://orcid.org/0000-0003-2025-3147
Rachael L. Beaton https://orcid.org/0000-0002-1691-8217
Gail Zasowski https://orcid.org/0000-0001-6761-9359
Julia O'Connell https://orcid.org/0000-0003-2321-950X
Dmitry Bizyaev https://orcid.org/0000-0002-3601-133X
D. A. García-Hernández https://orcid.org/0000-0002-1693-2721
Doug Geisler https://orcid.org/0000-0002-3900-8208
Henrik Jönsson https://orcid.org/0000-0002-4912-8609
Richard R. Lane https://orcid.org/0000-0003-1805-0316
Penélope Longa-Peña https://orcid.org/0000-0001-9330-5003
Ivan Minchev https://orcid.org/0000-0002-5627-0355
Dante Minniti https://orcid.org/0000-0002-7064-099X
Christian Nitschelm https://orcid.org/0000-0003-4752-4365
A. Roman-Lopes https://orcid.org/0000-0002-1379-4204

References

Abdurro'uf, Accetta, K., Aerts, C., et al. 2022, ApJS, 259, 35
Ahumada, R., Prieto, C. A., Almeida, A., et al. 2020, ApJS, 249, 3
Beaton, R. L., Oelkers, R. J., Hayes, C. R., et al. 2021, AJ, 162, 302
Bennett, M., & Bovy, J. 2019, MNRAS, 482, 1417
Blanton, M. R., Bershady, M. A., Abolfathi, B., et al. 2017, AJ, 154, 28
Bowen, I. S., & Vaughan, A. H. J. 1973, ApOpt, 12, 1430
Bragaglia, A., Sestito, P., Villanova, S., et al. 2008, A&A, 480, 79
Cantat-Gaudin, T., & Anders, F. 2020, A&A, 633, A99
Cantat-Gaudin, T., Jordi, C., Vallenari, A., et al. 2018, A&A, 618, A93
Cantat-Gaudin, T., Anders, F., Castro-Ginard, A., et al. 2020, A&A, 640, A1
Carrera, R., & Pancino, E. 2011, A&A, 535, A30
Casali, G., Magrini, L., Tognelli, E., et al. 2019, A&A, 629, A62
Casamiquela, L., Blanco-Cuaresma, S., Carrera, R., et al. 2019, MNRAS, 490, 1821
Castro-Ginard, A., Jordi, C., Luri, X., et al. 2022, A&A, 661, A118
Chiappini, C. 2009, IAUS, 254, 191
Cunha, K., Frinchaboy, P. M., Souto, D., et al. 2016, AN, 337, 922
Cunha, K., Smith, V. V., Hasselquist, S., et al. 2017, ApJ, 844, 145
Dias, W. S., Monteiro, H., Moitinho, A., et al. 2021, MNRAS, 504, 356

Donor, J., Frinchaboy, P. M., Cunha, K., et al. 2018, AJ, 156, 142
Donor, J., Frinchaboy, P. M., Cunha, K., et al. 2020, AJ, 159, 199
Drimmel, R., & Poggio, E. 2018, RNAAS, 2, 210
Foreman-Mackey, D., Hogg, D. W., Lang, D., & Goodman, J. 2013, PASP, 125, 306
Friel, E. D., Jacobson, H. R., & Pilachowski, C. A. 2010, AJ, 139, 1942
Frinchaboy, P., Zasowski, G., Jackson, K., et al. 2010, in JENAM 2010, Joint European and National Astronomy Meeting (Lisbon: JENAM), 136
Frinchaboy, P. M., Thompson, B., Jackson, K. M., et al. 2013, ApJL, 777, L1
Gaia Collaboration, Prusti, T., de Bruijne, J. H. J., et al. 2016, A&A, 595, A1
Gaia Collaboration, Brown, A. G. A., Vallenari, A., et al. 2021, A&A, 649, A1
García Pérez, A. E., Allende Prieto, C., Holtzman, J. A., et al. 2016, AJ, 151, 144
Gilmore, G., Randich, S., Asplund, M., et al. 2012, Msngr, 147, 25
Gravity Collaboration, Abuter, R., Amorim, A., et al. 2018, A&A, 615, L15
Gravity Collaboration, Abuter, R., Amorim, A., et al. 2021, A&A, 647, A59
Gunn, J. E., Siegmund, W. A., Mannery, E. J., et al. 2006, AJ, 131, 2332
Holtzman, J. A., Shetrone, M., Johnson, J. A., et al. 2015, AJ, 150, 148
Holtzman, J. A., Hasselquist, S., Shetrone, M., et al. 2018, AJ, 156, 125
Hubeny, I., Allende Prieto, C., Osorio, Y., & Lanz, T. 2021, arXiv:2104.02829
Hubeny, I., & Lanz, T. 2017, arXiv:1706.01859
Jacobson, H. R., Friel, E. D., Jílková, L., et al. 2016, A&A, 591, A37
Janes, K. A. 1979, ApJS, 39, 135
Jönsson, H., Holtzman, J. A., Allende Prieto, C., et al. 2020, AJ, 160, 120
Kounkel, M., Covey, K., & Stassun, K. G. 2020, AJ, 160, 279
Kounkel, M., Covey, K., Suárez, G., et al. 2018, AJ, 156, 84
Magrini, L., Randich, S., Kordopatis, G., et al. 2017, A&A, 603, A2
Majewski, S. R., Schiavon, R. P., Frinchaboy, P. M., et al. 2017, AJ, 154, 94
Martell, S. L., Sharma, S., Buder, S., et al. 2017, MNRAS, 465, 3203
Minchev, I., Chiappini, C., & Martig, M. 2013, A&A, 558, A9
Minchev, I., Chiappini, C., & Martig, M. 2014, A&A, 572, A92
Monteiro, H., & Dias, W. S. 2019, MNRAS, 487, 2385
Netopil, M., Oralhan, I. A., Çakmak, H., Michel, R., & Karataş, Y. 2022, MNRAS, 509, 421
Netopil, M., Paunzen, E., Heiter, U., & Soubiran, C. 2016, A&A, 585, A150
Nidever, D. L., Holtzman, J. A., Allende Prieto, C., et al. 2015, AJ, 150, 173
O'Connell, J. E. 2017, PhD thesis, Texas Christian Univ.
Osorio, Y., Allende Prieto, C., Hubeny, I., Mészáros, S., & Shetrone, M. 2020, A&A, 637, A80
Price-Whelan, A. M., Hogg, D. W., Johnston, K. V., et al. 2021, ApJ, 910, 17
Reddy, A. B. S., Lambert, D. L., & Giridhar, S. 2016, MNRAS, 463, 4366
Reid, M. J., & Brunthaler, A. 2004, ApJ, 616, 872
Sales-Silva, J. V., Daflon, S., Cunha, K., et al. 2022, ApJ, 926, 154
Santana, F. A., Beaton, R. L., Covey, K. R., et al. 2021, AJ, 162, 303
Seabroke, G. M., Fabricius, C., Teyssier, D., et al. 2021, A&A, 653, A160
Sestito, P., Bragaglia, A., Randich, S., et al. 2008, A&A, 488, 943
Shetrone, M., Bizyaev, D., Lawler, J. E., et al. 2015, ApJS, 221, 24
Smith, V. V., Bizyaev, D., Cunha, K., et al. 2021, AJ, 161, 254
Spina, L., Magrini, L., & Cunha, K. 2022, Univ, 8, 87
Spina, L., Ting, Y. S., De Silva, G. M., et al. 2021, MNRAS, 503, 3279
Spoo, T., Tayar, J., Frinchaboy, P. M., et al. 2022, AJ, 163, 229
Wilson, J. C., Hearty, F. R., Skrutskie, M. F., et al. 2019, PASP, 131, 055001
Yong, D., Carney, B. W., & Friel, E. D. 2012, AJ, 144, 95
Zasowski, G., Johnson, J. A., Frinchaboy, P. M., et al. 2013, AJ, 146, 81
Zasowski, G., Cohen, R. E., Chojnowski, S. D., et al. 2017, AJ, 154, 198
Zhang, H., Chen, Y., & Zhao, G. 2021, ApJ, 919, 52